Metallic Magnetic Calorimeters

A. Fleischmann[1], C. Enss[1], and G.M. Seidel[2]

[1] Kirchhoff-Institut für Physik, Universität Heidelberg, Im Neuenheimer Feld 227, D 69120 Heidelberg, Germany
andreas.fleischmann@kip.uni-heidelberg.de
[2] Physics Department, Brown University, Providence, RI 02912, USA

Abstract. Magnetic calorimeters employ the magnetization of a paramagnetic sensor to detect temperature changes produced by the absorption of X-rays or other energetic particles. For typical applications, the detector consists of a metallic absorber and a paramagnetic sensor, which are in strong thermal contact with each other but have a rather weak coupling to a thermal reservoir. The absorption of energy in the calorimeter leads to a rise in temperature and a decrease in magnetization of the magnetic sensor, which can be measured accurately using a low noise, high bandwidth dc-SQUID magnetometer. Fast thermal response can be achieved by using a dilute concentration of paramagnetic ions in a metallic host as sensor material. The sensitivity of the calorimeter to the absorption of energy depends upon size, heat capacity, temperature, magnetic field, concentration of magnetic ions and the interactions among them. Theoretical models, which describe the thermodynamic properties of the calorimeter are discussed, and the conditions that optimize the performance of the detector are derived. Noise sources, especially magnetic Johnson noise and thermodynamic fluctuations of energy between the sub-systems of the calorimeter are analyzed. We discuss the demands placed on the SQUID magnetometer and present a theoretical analysis of the energy resolution. The performance of detector prototypes, including count rate, linearity and energy resolution are described. The measured resolution of devices which were designed for the detection of soft X-rays is $E_{\mathrm{FWHM}} = 3.4\,\mathrm{eV}$ at an X-ray energy of 6 keV. Calculations indicate that fully optimized magnetic calorimeters will reach energy resolutions of the order of 1 eV under realistic experimental conditions.

1 Introduction

Thermometry based on the magnetic properties of solids has a long tradition in physics. The obvious reasons for this are that the magnetic properties of many materials are strongly dependent on temperature and that there exist very sensitive methods of measuring magnetization changes. In fact, the most sensitive thermometers in use today are magnetic in nature having a resolution of 1 part in 10^{10} [1, 2, 3, 4]. Therefore, it is not surprising that magnetic sensors are also used in micro-calorimetry. To our knowledge the idea of low-temperature magnetic calorimetry for particle detection was first mentioned in the diploma thesis of W. Seidel of the Technical University in Munich in 1986 [5]. Subsequently, a development effort of applying paramagnetism to particle detection was started at the Walther-Meissner-Institute in Munich.

Chr. Enss (Ed.): Cryogenic Particle Detection, Topics Appl. Phys. **99**, 151–217 (2005)

Within a few years, Umlauf and coworkers demonstrated the power of using the magnetization of $4f$ ions in a dielectric host material to measure small energy inputs to an absorber with a large heat capacity [6,7,8,9,10,11,12,13,14]. Despite this success, magnetic calorimeters based on dielectric host materials were not attractive for many applications in particle detection, because of their inherently slow response. This principal problem arises from the weak coupling of the magnetic moments to phonons at low temperatures.

In 1993 it was suggested that this problem can be overcome by using magnetic ions in metallic host materials [15]. In a metal the interaction of the magnetic moments with the conduction electrons leads to relaxation times many orders of magnitude shorter than in insulating hosts. The penalty for the faster response is that the presence of the conduction electrons increases the heat capacity of the sensor and in addition leads to an enhanced interaction among the magnetic moments. Nonetheless, metallic magnetic calorimeters (MMC) have exhibited excellent resolving power, comparable to that of other leading micro-calorimeters [16]. In this chapter we will focus on the discussion of metallic magnetic calorimeters.

A MMC employs a paramagnet placed in a small magnetic field as a temperature sensor. An absorber suitable for stopping the particle being detected is in strong thermal contact with the sensor. These two components are weakly coupled to a thermal bath. An energy deposition in the absorber produces a temperature change in the absorber/sensor system, which can be monitored by measuring the change of magnetization of the paramagnetic sensor using a sensitive dc SQUID magnetometer.

MMCs are different in several ways from other micro-calorimeters. Unlike detectors with resistive sensors, the signal of an MMC is not based upon a transport property but is determined by the equilibrium thermodynamic properties of the sensor material. Hence, the performance of MMCs can be predicted with some confidence. Two other differences are significant in certain uses. MMCs are non-dissipative devices, and no contact leads to the micro-calorimeter itself are necessary to read out the sensor. As we shall discuss, these differences are important in designing MMCs for particular applications.

Currently, the application of MMCs lies mainly in high resolution X-ray spectroscopy. Examples of uses are X-ray fluorescence spectroscopy for material analysis and absolute activity measurements of X-ray sources. In addition, a development effort has been started to build large arrays of magnetic micro-calorimeters for space based X-ray telescopes. There are many conceivable applications of MMCs beyond X-ray detection ranging from rare event searches in nuclear physics such as the neutrinoless double beta decay to the mass spectroscopy of biological molecules.

2 Theoretical and Experimental Background

In this section the physics of MMCs will be discussed that is necessary to describe and optimize their performance. In addition, we outline different techniques for readout and data analysis.

2.1 Detection Scheme

Similar to other micro-calorimeters, MMCs consist of an absorber, whose temperature is monitored with a sensitive thermometer. In the case of MMCs the temperature information is obtained from the change of magnetization of a paramagnetic sensor, which is located in a small magnetic field. From equilibrium thermodynamics the change of magnetization caused by the absorption of energy δE is given by the simple relation

$$\delta M = \frac{\partial M}{\partial T}\,\delta T = \frac{\partial M}{\partial T}\,\frac{\delta E}{C_{\mathrm{tot}}}\,, \tag{1}$$

where C_{tot} denotes the total heat capacity of thermometer and absorber. To measure the magnetization change the sensor is either placed in a pickup coil coupled to the input coil of a sensitive dc SQUID or is placed directly into the SQUID loop. The transfer function relating magnetization change to flux change in the SQUID depends, obviously, on the details of the geometry of the setup. This point will be discussed in Sect. 2.4.

2.2 Sensor Materials

The choice of sensor materials for a magnetic calorimeter is not trivial because the sensor needs to be optimized with respect to different and, in part, conflicting demands. For applications in particle detection the sensitivity and the thermalization time are of particular importance.

In terms of sensitivity cerium magnesium nitrate (CMN) is an obvious choice in the temperature range down to a few millikelvin. The magnetic dipole interaction between the Ce ions is particularly weak because of their location in a trigonal crystal structure and because of the highly anisotropic g-factor ($g_{\parallel} = 0.25$ and $g_{\perp} = 1.84$ [17]). As a consequence, magnetic ordering into a ferromagnetic state occurs for CMN only at very low temperatures ($T_{\mathrm{c}} \approx 1.9\,\mathrm{mK}$). This material has the advantage that the contribution to the heat capacity from interacting magnetic moments is very small despite the large spin concentration. However, the main drawback in using CMN, and other dielectric materials, as sensors in detectors arises from the extremely slow energy exchange between magnetic moments and phonons at very low temperatures. Spin-phonon relaxation times the order of seconds and longer are typical at millikelvin temperatures.

Notwithstanding the potential problem of long relaxation times, Umlauf and coworkers investigated the use of paramagnetic dielectrics for particle detection [6,7,8,9,10,11,12,13,14]. They used the compound Tm–Al–Garnet doped with 0.5% ^{168}Er attached to a 120 g Si absorber operated in a field of 3 mT at 30 mK and achieved an energy sensitivity of 320 eV in experiments with 5 MeV α particles [9]. Under optimal conditions the rise time of their signals was about 40 ms and the thermalization time with the bath was the order of 10 s. These values are unacceptably long for many applications in particle detection.

The principal problem of long relaxations times can be overcome by embedding the magnetic ions in metallic or semi-metallic host materials [15]. Here the strong coupling of the conduction electrons and the localized spins leads to rapid thermalization. Time constants for establishing thermal equilibrium within the sensor can be well below a microsecond.

The price one pays for this gain in detector speed is the additional heat capacity of the sensor and enhanced interaction between the localized magnetic moments via the Ruderman-Kittel-Kasuya-Yosida (RKKY) interaction because of the conduction electrons. This indirect exchange interaction has two undesirable consequences for the performance of magnetic calorimeters, namely an additional heat capacity associated with the exchange system and a reduction of the temperature dependence of the magnetization. Therefore, the system of choice is one with the smallest possible RKKY exchange interaction. Without exception, ions in the $4f$ rare earth series are better in this regard than those in the $3d$ and $4d$ transition metal series because of their weaker interaction with conduction electrons. Among the rare earth ions, those with a small de Gennes factor [18], $(g_J - 1)^2 J(J + 1)$, are preferable for the same reason. Here g_J denotes the Landé g-factor of the free ion and J total angular momentum.

Another aspect that needs to be considered in selecting the best magnetic ion for magnetic calorimeters is related with its nuclear properties. A nuclear spin can lead to an unwanted hyperfine contribution to the heat capacity and to a reduction of the magnetization at the magnetic fields in which the sensor operates.

Based on the reasons given above, erbium appears to be a particularly good candidate for the magnetic ion, with the exception of the isotope ^{167}Er, because of its nuclear spin (see Sect. 2.2.1).

In terms of metallic host system there are, in principle, a wide range of choices spanning from semi-metals, for example Bi_2Te_3, to noble metals such as gold. Semi-metals offer the advantage of having a much smaller conduction electron density and therefore a reduced exchange interaction. However, at this time very little is known about the properties of erbium in semi-metals, especially in terms of relaxation times, heat capacity, and magnetization. In addition, production and fabrication issues have to be studied before a judgment of their suitability as magnetic calorimeters can be determined.

For practical reasons most of the work to date has been done with gold as a host material and erbium as the magnetic ion. In addition to this alloy, LaB_6 doped with erbium [19], gold doped with ytterbium [20] and silver doped with erbium [21] have been investigated for use in metallic magnetic calorimeters. Since none of these materials have shown properties that are better than Au:Er we will concentrate in the following on this alloy.

2.2.1 Au:Er

Erbium in low concentrations forms a solid solution with gold. Erbium in the 3+ state substitutes for Au at regular fcc lattice sites giving three of its electrons to the conduction band. The Er^{3+} ion has the electron configuration $[Kr]4d^{10}4f^{11}5s^25p^6$. The paramagnetic behavior results from the partially filled $4f$ shell, having a radius of only about 0.3 Å and located deep inside the outer $5s$ and $5p$ shells. For comparison, the ionic radius of Er^{3+} is about 1 Å. Because of this the influence of the crystal field is greatly reduced and the magnetic moment can be calculated from the orbital angular momentum $\boldsymbol{L}$ the spin angular momentum $\boldsymbol{S}$ and the total angular momentum $\boldsymbol{J}$, which are derived according to Hund's rules. To a good approximation the admixture of exited electronic states can be neglected and the magnetic moment $\boldsymbol{\mu}$ can be written as

$$\boldsymbol{\mu} = g_J \boldsymbol{J} \tag{2}$$

with the Landé factor

$$g_J = 1 + \frac{J(J+1) + S(S+1) - L(L+1)}{2J(J+1)} \,. \tag{3}$$

For Er^{3+}, $L = 6$, $S = 3/2$, $J = 15/2$ and $g_J = 6/5$. In dilute Au:Er samples the magnetization can indeed be characterized by (2) at temperatures above about 100 K [22]. At lower temperatures it is necessary to include crystal field effects in the description. The crystal field with fcc symmetry lifts the sixteen-fold degeneracy of the Er^{3+} ground state, splitting it into a series of multiplets (one Γ_6 and one Γ_7 doublet and three Γ_8 quartets). The lowest lying multiplet is a Γ_7 Kramers doublet. At sufficiently low temperatures and low magnetic fields the behavior of erbium in gold can be approximated as a two level system with effective spin $\tilde{S} = 1/2$ with an isotropic g factor of $\tilde{g} = 34/5$. This theoretical value has been confirmed by several ESR experiments (see, for example [23]). The magnitude of energy splitting between the ground state doublet and the first excited multiplet (Γ_8 quartet) has been reported in different experiments [22, 24, 25, 26] to be between 11 K and 19 K .

Figure 1 shows the magnetic susceptibility of Au doped with 600 ppm Er in the temperature range between 100 µK and 300 K. The data have been obtained in three different experiments [27, 28]. While the data at high temperatures ($T > 100$ K) are in good agreement with the Curie law for $J = 15/2$

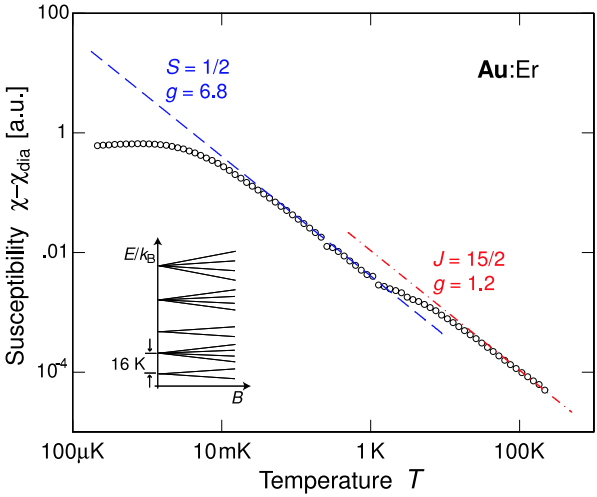

Fig. 1. Paramagnetic contribution to the magnetic susceptibility of Au containing 600 ppm Er as a function of temperature. The *two straight lines* represent the Curie susceptibility assuming Er^{+3} ions in the Γ_7-groundstate doublet and Er^{+3} ions without crystal field splitting. After [28]

and $g_J = 6/5$ there is an increasing deviation from the high temperature approximation below 100 K. This is a result of the depopulation of the multiplets with higher energies. At temperatures below about 1.5 K the data follow a Curie law once again, but with a reduced Curie constant in agreement with the effective spin $\widetilde{S} = 1/2$ and g factor $\tilde{g} = 6.8$ for the ground state doublet. At temperatures below 50 mK and in low magnetic fields such that saturation is unimportant ($\widetilde{g}\mu_B B < k_B T$), the susceptibility becomes much less temperature dependent. This is a result of the influence of the exchange interaction between the magnetic moments. Finally, at a temperature of about 0.9 mK a maximum in the magnetic susceptibility of the 600 ppm sample is observed, which is the result of a transition to a spin glass state.

Heat Capacity and Magnetization

The performance of a magnetic calorimeter based on Au:Er is determined by the heat capacity and the magnetization. Since the calorimeter is operated at very low temperature (10–100 mK) we include in the calculations only the ground state crystal-field doublet.

The heat capacity of a system of non-interacting spins is given by the well-known Schottky expression

$$C_s = N k_B \left(\frac{E}{k_B T}\right)^2 \frac{e^{E/k_B T}}{\left(e^{E/k_B T}+1\right)^2}\,, \tag{4}$$

which exhibits a maximum when the thermal energy $k_\mathrm{B}T$ is about half the energy splitting $E = \widetilde{g}\mu_\mathrm{B}B$. Here μ_B denotes the Bohr magneton. The magnetization of such a system is given by

$$M = \frac{N}{V}\,\widetilde{g}\widetilde{S}\mu_\mathrm{B}\mathcal{B}_\mathrm{s}(h) \tag{5}$$

with $h = \widetilde{g}\widetilde{S}\mu_\mathrm{B}/(k_\mathrm{B}T)$ and the Brillouin function

$$\mathcal{B}_\mathrm{s}(h) = \frac{2\widetilde{S}+1}{2\widetilde{S}}\,\coth\left(\frac{(2\widetilde{S}+1)h}{2\widetilde{S}}\right) - \frac{1}{2\widetilde{S}}\,\coth\left(\frac{h}{2\widetilde{S}}\right) \tag{6}$$

In the high temperature limit, $h \ll 1$, the magnetization varies as $1/T$ as expected for the Curie law.

While the assumption of non-interacting spins is sufficient for a qualitative description of the response of MMCs, it is inadequate for a quantitative analysis. To calculate the signal of a MMC both the magnetic dipole-dipole interaction and the indirect exchange interacting between the spins must be taken into account.

Because of the isotropy of the Γ_7 ground state doublet, the dipole–dipole interaction can be expressed in terms of the effective spins $\widetilde{S}_i$ and $\widetilde{S}_j$

$$H_{ij}^\mathrm{dipole} = \Gamma_\mathrm{dipole}\,\frac{1}{(2k_\mathrm{F}r_{ij})^3}\left[\widetilde{\boldsymbol{S}}_i\cdot\widetilde{\boldsymbol{S}}_j - 3\left(\widetilde{\boldsymbol{S}}_i\cdot\widehat{\boldsymbol{r}}_{ij}\right)\left(\widetilde{\boldsymbol{S}}_j\cdot\widehat{\boldsymbol{r}}_{ij}\right)\right] \tag{7}$$

with prefactor $\Gamma_\mathrm{dipole} = (\mu_0/4\pi)\,(\widetilde{g}\mu_\mathrm{B})^2\,(2k_\mathrm{F})^3$. The quantity $\widehat{\boldsymbol{r}}_{ij}$ represents the unit vector in direction $\boldsymbol{r}_i - \boldsymbol{r}_j$ and k_F the Fermi wave vector of the gold conduction electrons.[1]

The exchange interaction of the localized $4f$ electrons of the erbium ions with the gold conduction electrons gives rise to an additional interaction between the erbium ions, the indirect exchange or Ruderman-Kittel-Kasuya-Yosida (RKKY) interaction. Expressed in terms of the effective spin, the RKKY interaction between two erbium spins can be written as

$$H_{ij}^\mathrm{RKKY} = \Gamma_\mathrm{RKKY}\,(\widetilde{\boldsymbol{S}}_i\cdot\widetilde{\boldsymbol{S}}_j)\,F(2k_\mathrm{F}r_{ij}) \tag{8}$$

with the function $F(2k_\mathrm{F}r_{ij})$ being

$$F(2k_\mathrm{F}r_{ij}) = \frac{1}{(2k_\mathrm{F}r_{ij})^3}\left[\cos(2k_\mathrm{F}r_{ij}) - \frac{1}{2k_\mathrm{F}r_{ij}}\sin(2k_\mathrm{F}r_{ij})\right] \tag{9}$$

and prefactor Γ_RKKY given by

$$\Gamma_\mathrm{RKKY} = \mathcal{J}^2\,\frac{4V_0^2 m_\mathrm{e}^* k_\mathrm{F}^4}{\hbar^2(2\pi)^3}\,\frac{\widetilde{g}^2(g_J-1)^2}{g_j^2}\,. \tag{10}$$

[1] The Fermi wave vector has been introduced artificially here to simplify the quantitative comparison with the indirect exchange interaction discussed later

Here $\mathcal{J}$ denotes the coupling energy between the localized spins and the conduction electrons, V_0 is the volume of the elementary cell and m_e^* is the effective mass of the conduction electrons. The expression for the RKKY interaction given above is derived under the assumption that the mean free path of the electrons is larger than the mean distance between the localized erbium ions. In principle, it is possible that the RKKY interaction is reduced due to a finite coherence length λ of the spin polarization of the conduction electrons. In this case an additional factor $e^{-r/\lambda}$ would appear in (8). However, for Au:Er with suitable erbium concentrations for a MMC, the mean free path of the conduction electrons is always much larger than the mean separation of the erbium ions[2].

The fact that both the dipole-dipole interaction and the RKKY interaction are proportional to $1/r_{ij}^3$ allows us to compare their relative strength by a dimensionless parameter which is defined as the ratio of the two pre-factors

$$\alpha = \Gamma_{\mathrm{RKKY}}/\Gamma_{\mathrm{dipole}}\,. \tag{11}$$

Using this parameter α the coupling energy $\mathcal{J}$ can be expressed as[3]

$$\mathcal{J} \simeq \sqrt{\alpha}\,0.145\ \mathrm{eV}\,. \tag{12}$$

A determination of the heat capacity and magnetization of a system of randomly distributed, interacting erbium spins requires a numerical calculation. There is a number of ways to perform this kind of calculation in the framework of a mean-field approximation. The method that requires the least amount of CPU time assumes the specific form of the mean field distribution that has been derived by *Walker* and *Walstedt* [29,30] for magnetic moments randomly distributed in a continuous medium. These authors showed that this analytic representation of the mean field distribution agrees well with numerically calculated mean field distributions.

An alternative approach is to write down the Hamiltonian for a cluster of interacting, randomly distributed spins on the Au lattice and obtain the eigenvalues of the cluster. This process is repeated for a large number of configurations of randomly positioned spins with the heat capacity and magnetization obtained by averaging. The number of spins that should be included in a cluster and the number of different configurations of clusters that must be employed in the calculation depends upon the Er concentration. For concentrations the order of 1000 ppm at least 10^4 configurations of

[2] In measurements of the residual resistivity of dilute $Au_{1-x}Er_x$ alloys $\varrho = x\,6.7 \times 10^{-6}\,\Omega\,\mathrm{m}$ was found [31], and one can conclude that the mean free path of the conduction electrons is about 4000 Å for an erbium concentration of 300 ppm

[3] The value of $\mathcal{J}$ given by (12) refers to the definition of the exchange energy between a localized spin $\boldsymbol{S}$ and a free electron $\boldsymbol{s}$ being $H = \mathcal{J}\boldsymbol{s}\cdot\boldsymbol{S}$. The definition $H = 2\mathcal{J}\boldsymbol{s}\cdot\boldsymbol{S}$ is often found in the literature, leading to values of the parameter $\mathcal{J}$ being smaller by a factor of two

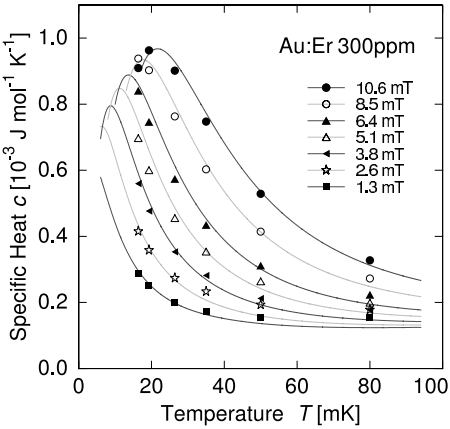

Fig. 2. Specific heat of Au:Er with 300 ppm enriched ^{166}Er as a function of temperature at different applied magnetic fields. The *solid lines* are calculated numerically with a interaction parameter $\alpha = 5$ [32]

clusters containing up to six spins are required to obtain a meaningful result. Clearly this procedure requires a large amount of CPU time, but the results are potentially more accurate than can be obtained from a mean field calculation. The interaction among spins in this method can employ the full Heisenberg Hamiltonian rather than the Ising approximation.

The appropriate averages over the results for different configurations have to be calculated. In case of Au:Er with moderate Er concentration this method provides a description the measured specific heat and magnetization rather well.

As an example we show in Fig. 2 the specific heat of an Au:Er sample having a concentration of 300 ppm of 97.8% enriched ^{166}Er. The temperature of the maximum in the specific heat depends on the magnitude of the external magnetic field as expected for a Schottky anomaly. However, the maximum is about twice as wide as for a non-interacting spin system. Calculations based on averaging over spin clusters provides a quantitative agreement assuming a interaction parameter α of 5. Although the calculated curves depend rather strongly on the choice of α, the value of $\alpha = 5$ should be viewed as a upper bound for the following two reasons. Firstly, the presence of ^{167}Er in the enriched sample leads to a slight additional broadening of the curve because of the hyperfine contribution of this isotope. Secondly, additional broadening results from a variation of the applied magnetic field, of about 10 to 15%, over the sample due to the geometry of the field coil.

The magnetization is plotted as a function of $1/T$ in Fig. 3 at several different magnetic fields for the 300 ppm sample. As in the case of the specific heat, the magnetization deviates for the behavior of isolated spins. The deviation is primarily due to the interaction between the magnetic moments, but

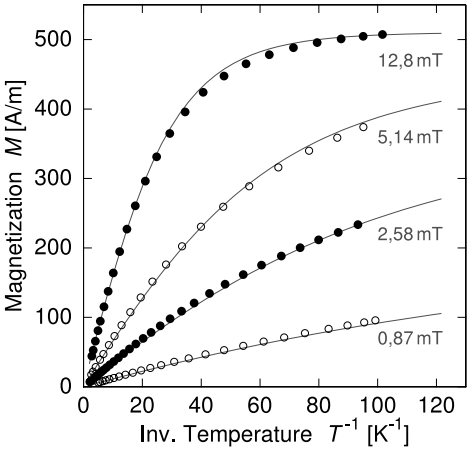

Fig. 3. Magnetization of Au:Er with 300 ppm enriched ^{166}Er as a function of $1/T$ at different applied magnetic fields. The *solid lines* are calculated numerically with a interaction parameter $\alpha = 5$ [32]

a small contribution is also present due to the two reasons discussed above for the heat capacity. Again the data can be described satisfactorily by assuming an interaction parameter of $\alpha = 5$.

The magnetic properties of a weakly interacting spin system is perhaps most easily characterized in terms of the temperature dependence of the susceptibility given by the Curie-Weiss law, $\chi = \lambda/(T+\theta)$. The Curie constant λ is proportional to the concentration of the spins, as is the Weiss constant θ, which is a measure of strength of the interactions. For the Au:Er system, $\lambda = x\,5.3\,\mathrm{K}$ and $\theta = \alpha\,x\,1.1\,\mathrm{K}$.

Response Time

A fast response time can be very important for calorimeters used as particle detectors. This is the main reason why metallic paramagnets such as Au:Er are chosen over dielectric compounds. The strong conduction electron-spin interaction in metallic paramagnets produces response times in the microsecond range even below 50 mK. Obviously, the response time of the calorimeter is not only determined by the properties of the sensor material, but by the choice of the absorber and the thermal connection between the two components. The only way to insure the fast response of the sensor is to employ a metal or semi-metal as absorber and to bond the absorber and sensor together in such a way that the conduction electrons carry the heat across the interface.

The absorption of an X-ray occurs primarily via the photoelectric effect resulting in the generation of an energetic electron. This electron loses its energy rather quickly by electron-electron scattering. After about 10^{-13} s the

mean energy of the athermal electrons is reduced to about 0.1 eV. At this energy the athermal electrons lose their energy predominately by the generation of high-frequency phonons. Subsequently, these high-frequency phonons thermalize via interaction with the conduction electrons. As the phonon and electron systems further thermalize most of the energy is returned into the electron system because of the larger heat capacity of conduction electrons at low temperature. By the time the local electron temperature has reached about 1 K the absorbed energy is distributed within a volume of a few cubic micrometers. The further thermalization within the absorber can be described by thermal diffusion. The time scale for this process is mainly determined by the geometry of the absorber and the presence of defects such as grain boundaries and dislocations. If we assume, for example, a pure gold absorber with dimensions $250\,\mu\text{m} \times 250\,\mu\text{m} \times 5\,\mu\text{m}$ having a resistance ratio of only $R_{300\,\text{K}}/R_{4\,\text{K}} \approx 3$, the thermalization time, using the Wiedemann–Franz law, can be estimated to be 10^{-7} s.

The time for the heat to flow from the absorber into the sensor is difficult to estimate since this depends very much on the nature of the thermal connection between the two components. By spot welding the gold absorber and Au:Er sensor together the contact can be made sufficiently strong that no degradation of the response time of the magnetic calorimeters due to the presence of the interface is observable.

Finally, the energy is shared with the magnetic moments in the sensor material giving rise of the signal. The response time of the spins is determined by the electron-spin relaxation time τ, which is described by the Korringa relation $\tau = \kappa/T$, where κ denotes the Korringa constant. For Au:Er the Korringa constant has been determined in ESR measurements at 1 K to be $\kappa = 7 \times 10^{-9}$ Ks [24]. This value of κ yields a spin-electron relaxation time of less than 10^{-7} s at 50 mK.

Influence of Nuclear Spins

In the design of a magnetic calorimeter the possible influence of nuclear spins has to be considered. In the case of Au:Er there a two ways in which nuclei can affect the performance of the calorimeter. Firstly, the isotope ^{167}Er with nuclear spin $I = 7/2$ influences the magnetization and the heat capacity due to its hyperfine interaction with the $4f$ electrons. Secondly, and more subtle, the 100% abundant ^{198}Au nuclei with small magnetic moment but large quadrupole moment may contribute to the specific heat if the nuclei reside at positions where the electric field gradient is of non-cubic symmetry.

We consider first the hyperfine contribution of the erbium isotope ^{167}Er having a natural abundance of 23%. This isotope, embedded in gold, has been investigated in ESR measurements [24]. From these measurements the hyperfine coupling constant is determined to be $A/k_\text{B} = -0.0335$ K, which results in zero magnetic field in a splitting of the energy levels into a doublet separated by 140 mK. In addition, the apparent nuclear g factor is found to

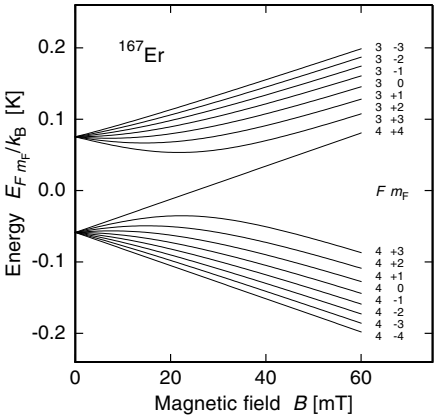

Fig. 4. Energy eigenvalues of the Γ_7-Kramers doublet of ^{167}Er in Au as a function of the applied magnetic field

be strongly enhanced by internal fields to the value of $g_N = -29$. Using these results the level scheme of the Γ_7 Kramers doublet can be calculated as a function of applied magnetic field. At low fields, as shown in Fig. 4, there are two groups of levels associated with the angular momentum quantum numbers $F = 3$ and $F = 4$.

In the temperature and magnetic field range of interest for the operation of MMCs, the magnetization and heat capacity of ^{167}Er ions is considerably different from that of Er isotopes with nuclear spin zero. The magnetization is reduced and the heat capacity enhanced. The specific heat of Au:Er sample with 480 ppm erbium with natural isotopic abundance at different applied magnetic fields is shown in Fig. 5. At low fields there are two distinct maxima visible. The one at low temperatures is caused by transitions within the $F = 4$ multiplet and by the contributions of isotopes with zero nuclear spin. The temperature at which this maximum occurs depends strongly on the magnetic field. In contrast, the broad maximum at higher temperatures ($T \approx 55$ mK) is nearly independent of magnetic field. It is caused by a redistribution in the population of spins between the two multiplets. At 10 mT and 50 mK this contribution makes up about 50% of the total specific heat. For maximum sensitivity it is necessary to eliminate this unwanted contribution by working with erbium deleted in the isotope ^{167}Er.

Nuclei of the host metal can also influence the performance of an MMC. The ^{198}Au nuclei have spin $I = 3/2$, a quadrupole moment of 0.547 barn and a magnetic moment sufficiently small to be neglected. In pure gold no contribution of the nuclear spins to the specific heat is expected at low fields, since the electric field of cubic symmetry does not lift the degeneracy of the nuclear levels. However, for Au nuclei in the vicinity of an Er^{3+} ion the electric field gradient can be substantial and can split the nuclear levels. This results

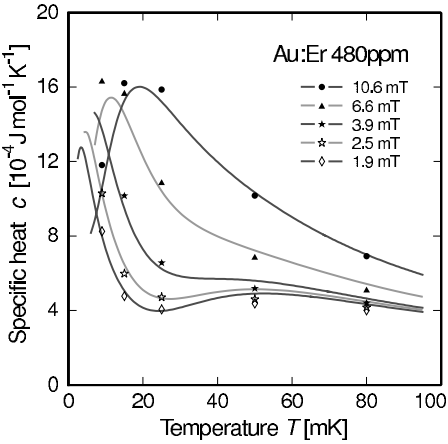

Fig. 5. Specific heat of Au:Er with 480 ppm of erbium with natural isotope abundance [33]

in an additional heat capacity. Fig. 6 shows the measured heat capacity of the Au nuclei as a function of temperatures for samples with different erbium concentrations. The data below 10 mK for the sample with 600 ppm is the total specific heat since at such low temperatures the contribution of the Au nuclei is substantially larger than that of all other degrees of freedom. The figure also shows a theoretical curve calculated assuming a quadrupole splitting of 70 MHz for Au nuclei in the immediate vicinity of erbium ions, the splitting decreasing for nuclei at larger distances in a manner similar to that measured in other dilute alloys such as Cu:Pt [34], Cu:Pd [35], and Gd:Au [36].

This unwanted contribution to the specific heat can only be eliminated by using a host material which has a nuclear spin $I \leq 1/2$. At first glance it would appear desirable to use silver as a host material rather than gold since the two isotopes of silver (^{107}Ag and ^{109}Ag) both have nuclear spin $I = 1/2$. However, the exchange energy J is 1.6 larger in silver than in gold as determined by ESR measurements[23]. Since the interaction parameter α is quadratic in the exchange energy $\alpha \propto J^2$, silver is not an attractive choice as a host material for a magnetic sensor.

2.3 Scaling

The behavior of systems of dilute concentrations of magnetic ions in metals interacting via the RKKY mechanism have been studied for many years. One property possessed by such systems is that of scaling [37], of which we shall make use in discussing the optimization of the design of MMCs in Sect. 2.4. Scaling, in the context of magnetic ions in metals, is the property that the dependence of thermodynamic quantities on magnetic field and temperature

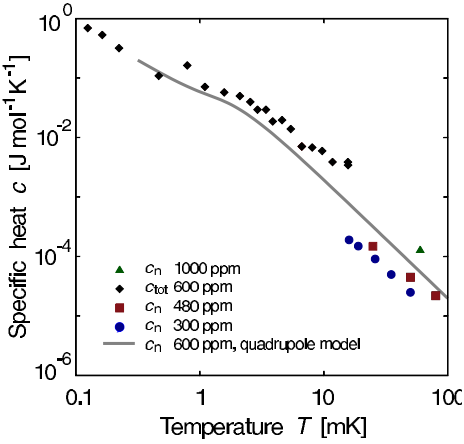

Fig. 6. Contribution of the Au nuclei to the specific heat of Au:Er samples with different concentrations. The *solid line* represents a theoretical curve assuming a quadrupole splitting of 70 MHz for Au nuclei, that are nearest neighbors of Er. Here c_{tot} denotes the total specific heat and c_{n} the contribution of just the Au nuclei to the specific heat. After [32]

at different concentrations are related to one another in a very simple way. The magnetization and heat capacity at a given B and T, for example, at one concentration are the same as that at another concentration at a field and temperature scaled by the ratio of the different concentrations. We outline the well known argument briefly below.

The effective field on a magnetic ion resulting from interactions with all surrounding ions through the RKKY coupling, given by (8), can be expressed as

$$B_i = \mathcal{A} \sum_{j>i} \frac{\cos(2k_{\mathrm{F}} r_{ij}) - \sin(2k_{\mathrm{F}} r_{ij})/(2k_{\mathrm{F}} r_{ij})}{(2k_{\mathrm{F}} r_{ij})^3} \,. \tag{13}$$

The prefactor $\mathcal{A}$ depends on Γ_{RKKY} as it is defined in (8) to (10). The probability distribution of fields, obtained by calculating B_i for all possible random arrangements of magnetic ions, is the quantity of interest in computing the thermodynamic properties of the system.

For dilute concentrations the separation between ions is much larger than the inverse of the Fermi wavevector, the factor $2k_{\mathrm{F}} r_{ij}$ is large, and the term containing the sine function in (13) can be neglected. Also for dilute concentrations, the cosine function oscillates in space with a wavelength that is very short compared to the spacing of the magnetic ions. As a consequence, the probability distribution of fields does not depend on the wavelength of oscillation, or, to invert the argument, the concentration dependence of the field distribution is independent of the cosine function. In considering the dependence of B_i on concentration, therefore, the oscillatory terms in the

numerator of (13) are irrelevant. But since the product, xr^3, of concentration and cube of inter-ion spacing, which appears in the denominator of (13), is independent of concentration, then, $B_i/x \propto \sum 1/(xr_{ij}^3)$ is independent of x as well. The fields B_i' at one concentration can be obtained from the fields B_i at another concentration by the relation $B_i' = nB_i$ where $n = x'/x$. The probability distribution of fields at a concentration x' and applied field B is, then, $P(B + nB_i) = nP(B/n + B_i)$. The distribution is a function of B/n.

In the mean field approximation, with the energy of an ion given by $\mathcal{E} = g\mu_B(B + nB_i)m_S$, the partition function is

$$\begin{aligned} Z(B,T,n) &= \prod_i P(B+nB_i) \sum_{m_S} \exp\left(\frac{-g\mu_B(B+nB_i)m_S}{k_BT}\right) \\ &= \prod_i n\,P(B/n+B_i) \sum_{m_S} \exp\left(\frac{-g\mu_B(B/n+B_i)m_S}{k_BT/n}\right). \end{aligned} \tag{14}$$

Hence,

$$Z(B,T,n) = nZ\left(\frac{B}{n}, \frac{T}{n}\right). \tag{15}$$

The dependence of thermodynamic functions on B and T all scale with concentration as B/n and T/n.

2.4 Optimization of Signal-to-SQUID-Noise Ratio

The magnitude of the output signal of a SQUID circuit measuring the response of a magnetic calorimeter depends on a number of parameters that are related to the calorimeter itself, to the measuring circuit, and to the coupling of the calorimeter to the circuit. In general, one wants to optimize the performance of a calorimeter, having a particular set of operating constraints, by maximizing the signal-to-noise ratio. We discuss the considerations associated with the process of optimization below.

The discussion in Sect. 2.2.1 of the thermodynamic properties of Au:Er suggests that the magnetic response of an MMC can be calculated either by computer simulations or analytically using mean field approximations. This ability to calculate the response provides a means of designing calorimeters that have the largest output signal per unit of energy input. Since the noise performance of SQUIDs is often characterized in terms of magnetic flux noise, we start our discussion of signal size in terms of flux that is generated in the sensing inductance of the magnetometer for a given energy deposition. Later we include the noise of the SQUID to optimize the overall performance by maximizing the signal-to-noise ratio.

2.4.1 Basic Ideas

Up to now we have described the response of the calorimeter by (1), $\delta m = V(\partial M/\partial T)(\delta E/C_{\rm tot})$. This expression suggests that the temperature sensor

should be made out of a magnetic material having a small heat capacity and large dependence of magnetization on temperature. Let us, for the moment, neglect any other contribution to the heat capacity of the calorimeter except for that of the spins. For non-interacting spins the quantities $\partial M/\partial T$ and c, the specific heat per unit volume of the spins, are related by the thermodynamic expression $\partial M/\partial T = c/B$. In this simple case

$$\delta m = \frac{\delta E}{B} \,. \tag{16}$$

A picture of the physics described by this relation can be obtained by noting the occupation numbers of the energy levels of the spins. For an ensemble of non-interacting spins with $S = 1/2$, the Zeeman energy splitting of the levels is $E_\mathrm{Z} = g\mu_\mathrm{B}B$. A deposition of energy δE induces a change in the number of spins $\delta N = \delta E/E_\mathrm{Z}$ from the lower to the upper energy level. The resulting change in the magnetic moment of the ensemble is, then, $\delta m = \delta N g\mu_\mathrm{B} = \delta E/B$, which is (16). For a typical magnetic field of $B = 10\,\mathrm{mT}$ and $g = 6.8$, the Zeeman splitting is $E_\mathrm{Z} \simeq 4\,\mu\mathrm{eV}$. In the energy regime MMCs are expected to be used the large number of excitations precludes statistical fluctuations in their number being a factor limiting the energy resolution.

If a sample of non-interacting spins were placed inside a circular loop of wire of radius r, the flux change resulting from a change of magnetization within it is given by

$$\delta\Phi = \mu_0 \frac{G}{r} \delta m \,, \tag{17}$$

where μ_0 is the magnetic permeability of free space and G is a dimensionless factor that depends on the geometry of the spins within the loop. For spins restricted to a small volume at the center of the loop $G = 1/2$. The combination of (16) and (17) lead to strategies for maximizing the signal size, which, in principle, are applicable to the discussion in the remainder of this article. 1. Since the coupling of a magnetic moment to a wire decreases with distance between them, the spins should be placed as close to the wire of the magnetometer as possible. And 2. the external field should be as small as possible so as to increase δm. However, as we now discuss, using a simple model, there are other factors that limit how low the field can profitably be made. The heat capacity of the calorimeter must include that of the absorber as well as that of the spins. If C_a describes the heat capacity of the absorber and non-spin degrees of freedom of the sensor (e.g. electrons, lattice), then only the fraction $\beta = C_\mathrm{s}/(C_\mathrm{s} + C_\mathrm{a})$ of the deposited energy reaches the spin system, C_s. The flux change in a circular loop, again for non-interacting spins, is

$$\delta\Phi = \mu_0 \frac{G}{r} \frac{C_\mathrm{s}}{C_\mathrm{s} + C_\mathrm{a}} \frac{\delta E}{B}. \tag{18}$$

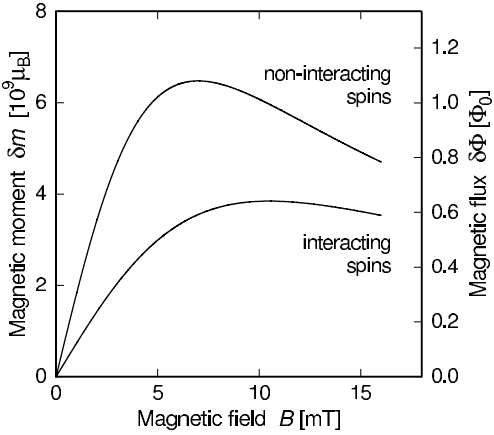

Fig. 7. Signal size of a magnetic calorimeter with an absorber heat capacity of $C_a = 1.1\,\mathrm{pJ/K}$ as a function of magnetic field in the case of interacting and non-interacting spins. The detector parameters assumed for calculating these curves are described in the text

At small fields such that $E_Z \ll k_B T$, $C_s \propto B^2$ for non-interacting spins, and the signal size, $\delta\Phi$, increases linearly with magnetic field in the low-field limit. Provided there are a large enough number of spins[4], the signal size has a maximum where $C_s(B) = C_a$ and decreases at higher field proportional to B^{-1}.

The calculated dependence of change in magnetic moment on magnetic field assuming non-interacting spins is illustrated by the *upper curve* on the *left vertical axis* in Fig. 7. The parameters for the calculated curve are $\delta E = 5.9\,\mathrm{keV}$, $T = 50\,\mathrm{mK}$, and $C_a = 1.1\,\mathrm{pJ/K}$, which corresponds to the heat capacity of a gold absorber $250 \times 250 \times 5\,\mu\mathrm{m}^3$ at this temperature. The sensor is assumed to be a cylindrical disc having a diameter $52\,\mu\mathrm{m}$ and height of $6.5\,\mu\mathrm{m}$, made of 900 ppm Au:Er. The calculated change in magnetization has a maximum at a field of about 7 mT, which corresponds to the heat capacity of the spins being approximately equal to that of the absorber, as expected from the discussion above.

The *right vertical axis* shows the corresponding change in flux in a circular loop where the loop is taken to be made of a thin film of superconducting niobium having an inner radius equal to the radius r of the sensor and a width w of the niobium $w = 0.1r$. The coupling factor, G, depends on both the geometry of the sensor and that of the loop. In Fig. 10a the coupling factor is plotted as a function of the ratio $\xi = h/2r$ for both an infinitely thin loop and for the value $w = 0.1r$ used in calculating the flux plotted in Fig. 7.

[4] In order to stay within the small field approximation, the heat capacity of the spins at the maximum of the Schottky anomaly must be larger than the additional heat capacity C_a

What has been left out of the discussion to this point are the interactions among the spins, which can have a significant influence not only on the magnitude of the response but also on the dependence of the response on parameters such as temperature and field. The *lower curve* in Fig. 7 is the calculated dependence of the change in magnetic moment including dipole-dipole and RKKY interactions with $\alpha = 5$. All other parameters are the same as used for the non-interacting case. The effect of the interactions is to reduce the response and to shift the maximum to somewhat higher fields. The reduction can be understood in that the interactions increase the heat capacity and decrease the temperature dependence of the magnetization.

We are now at a point where we need to consider the optimization of the performance of a magnetic calorimeter, including the noise of the magnetometer used to read out the paramagnetic sensor. That discussion is outlined in the following sections for the case of a cylindrical sensor in a circular loop, being followed by an extension of the arguments to the case of planar sensors with pickup coils of meander shape.

2.4.2 SQUID-based sensor readout

In this section we review several properties of dc-SQUIDs that will later be used in discussing the signal-to-SQUID-noise ratio of magnetic calorimeters. For a detailed discussion of the properties and the fabrication of SQUIDs we refer to [38] and the references therein.

Dc-SQUIDs are the most sensitive devices for monitoring the magnetization of the paramagnetic sensors of MMCs. For an MMC to have the highest possible energy resolution it should be read out with a SQUID having low noise and high dynamic range. A dc-SQUID can be operated with reasonably small power dissipation ($P < 1\,\mathrm{nW}$) at very low temperatures ($T \leq 4.2\,\mathrm{K}$), thereby permitting the fabrication of integrated detectors working at temperatures of a few tens of millikelvin.

A dc-SQUID can be used as a sensitive flux-to-voltage converter. Figure 8a shows a schematic drawing of a dc-SQUID, consisting of a superconducting loop of wire, which is interrupted by two Josephson contacts marked by crosses. Each Josephson contact acts as a weak link between the adjacent superconductors. This region of suppressed superconductivity is small enough that Cooper pairs can tunnel through it. The small distance between the electrodes of each contact results in a parasitic capacitance denoted as C. Each junction is shunted by a resistor R in order to suppress hysteretic behavior of the device.

If small currents are driven though the device, the current can be carried by tunneling Cooper pairs without dissipation. However, if the device is biased at a current close to two times the critical current of *one* junction, a voltage drop develops across the device. Due to the Josephson effect, the dc-voltage across the device depends periodically on the magnetic flux through the inductance L_s of the SQUID, where the periodic flux range is given by

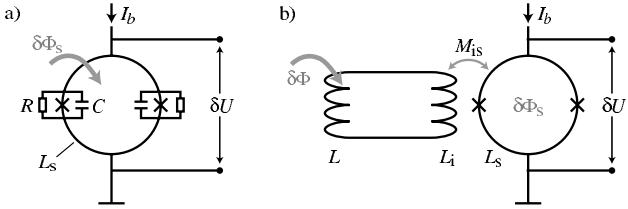

Fig. 8. Schematic of a dc-SQUID, where the flux to be measured is (**a**) directly coupled to the sensing inductance of the SQUID, (**b**) coupled to the SQUID via a superconducting flux transformer

one flux quantum $\Phi_0 = h/2e = 2.07 \times 10^{-15}\,\mathrm{Vs}$. Operated at a steep point of this flux-voltage characteristic, the device can be used as a sensitive flux-to-voltage converter. A flux-locked-loop electronics, which applies negative feedback to compensate the flux change resulting from a signal, is often used in order to linearize the flux-voltage characteristic of the SQUID.

The shunt resistors R, which are needed for damping, cause current and voltage noise, and limit the apparent flux sensitivity of the SQUID. The spectral power density of flux noise $S_{\Phi\mathrm{s}}$ as well as the energy sensitivity ϵ_s are frequently used parameters to characterize the noise of a dc-SQUID, the relation between the two being

$$\epsilon_\mathrm{s} = \frac{S_{\Phi\mathrm{s}}}{2L_\mathrm{s}}\,. \tag{19}$$

The knowledge of the dependence of these quantities, ϵ_s and $S_{\Phi\mathrm{s}}$, on the inductance of the SQUID is important for optimizing the energy resolution of MMCs, as we shall discuss in the next section.

As discussed in [38], it is difficult in practice to give a simple relation of the dependence of SQUID noise on inductance. Many parameters, such as the parasitic capacitance and the critical current, may be constrained by the requirements of the fabrication process so as to provide for high yield and reproducibility. Taking the junction capacity of the fabrication process to be the limiting parameter, and assuming an optimal value for the resistive shunt R, one can express the optimum energy sensitivity of a dc-SQUID as

$$\epsilon_\mathrm{s} \simeq 16 k_\mathrm{B} T \sqrt{L_\mathrm{s} C}\,. \tag{20}$$

The relation suggests that the flux noise $\sqrt{S_{\Phi\mathrm{s}}}$ increases with increasing SQUID inductance as $\sqrt{S_{\Phi\mathrm{s}}} \propto L_\mathrm{s}^{3/4}$. However, in the low-temperature limit the energy resolution of a SQUID should ultimately reach the quantum limit, $\epsilon_\mathrm{s} \geq \hbar$, leading to $\sqrt{S_{\Phi\mathrm{s}}} \propto \sqrt{L_\mathrm{s}}$. When optimizing the signal-to-SQUID-noise ratio in the following sections, we shall use this dependence of the flux noise in the pickup loop on its inductance, although we are not aware of any work on magnetic sensors where the quantum limited operation of SQUIDs has been encountered.

The use of $\sqrt{S_{\Phi s}} \propto \sqrt{L_s}$ is also consistent with the following argument. Assume the change in flux in a sensor is read out by a superconducting coil with inductance L, which forms a completely superconducting circuit with a second coil L_i coupled by mutual inductance to a SQUID, as illustrated in Fig. 8b. For clarity, capacitance and shunt resistor have been omitted in Fig. 8b. The combination of a SQUID and a strongly coupled input coil L_i is usually called a current-sensor SQUID. The circuit formed by L and L_i is often called a flux transformer, because a change of magnetic flux $\delta\Phi$ in the pickup coil L causes the flux in the SQUID to change by

$$\delta\Phi_s = \frac{k\sqrt{L_s L_i}}{L + L_i}\,\delta\Phi \leq \frac{1}{2}\sqrt{\frac{L_s}{L}}\,\delta\Phi\,. \tag{21}$$

Here $k\sqrt{L_s L_i} = M_{is}$ denotes the mutual inductance between the input coil and the SQUID. The dimensionless coupling constant k can have a value close to unity for SQUIDs fabricated by a multi-layer niobium thin-film process. Best coupling is achieved, corresponding to the equal sign in the relation on the right, if the inductance L_i of the input coil equals the inductance L of the pickup coil.

Assuming best coupling, we can describe the flux noise referred to the pickup coil by

$$\sqrt{S_\Phi} = \sqrt{2L\epsilon} \geq 2\sqrt{2L\epsilon_s}\,, \tag{22}$$

where ϵ and ϵ_s represent the energy sensitivity referred to the pickup coil and to the SQUID[5], respectively. The equal sign in the last relation is achieved if $k = 1$. Two points are worthy of note. 1. If a SQUID has a fixed energy sensitivity with a well coupled input coil, whose inductance L_i can be varied over a reasonably large range, then the flux noise referred to a transformer-coupled pickup coil is proportional to the square root of its inductance, $\sqrt{S_\Phi} \propto \sqrt{L}$. Therefore, when optimizing the signal-to-SQUID-noise ratio of MMCs in the next section we shall maximize the change of flux in a pickup up coil per energy input in the detector and per square root of pickup coil inductance. 2. The energy sensitivity of a transformer-coupled pickup coil is about 4 times worse than the energy sensitivity of the SQUID. However, there are situations where this loss in sensitivity may be compensated by other benefits of transformer-coupled sensor readout. Firstly, the fabrication of SQUIDs with good energy sensitivity becomes increasingly difficult with increasing SQUID inductance. In cases where the inductance of the preferred pickup

[5] In this configuration the energy sensitivity ϵ_s of the SQUID might be reduced due to a reduction of self inductance of the SQUID, which is caused by the screening current in the flux transformer. In the case of best coupling, $L = L_i$, this effect should in first order be independent of the input inductance L_i and therefore does not change the qualitative dependence of flux noise on inductance discussed here

coil is rather large, *i.e.*, $L \gg 100\,\mathrm{pH}$, transformer coupling may even lead to the smaller effective flux noise. Secondly, transformer coupling allows for a spatial and thermal separation of sensor and SQUID. This may be very helpful in the context of large detector arrays consisting of several thousand pixels. Low noise readout of a dc-SQUID requires a power of 10 pW to 1 nW to be dissipated in the SQUID. This power is in part transformed into heat in the shunt resistors, and in part radiated at the Josephson frequency and higher harmonics, leading to eddy-current heating in the sensor. The use of unshunted SQUIDs [39] may help to reduce the heat from dissipation in the shunt resistors, but handling the residual heat load on a silicon chip at millikelvin temperatures becomes increasingly hard with an increasing number of detectors. Having SQUIDs and sensors on separate chips with appropriate filters in the interconnects appears to be a means of handling this problem, as the power dissipation on the sensor chip can be made almost arbitrarily small in this configuration.

In the remainder of this section we discuss a few of the possible sensor/SQUID coupling schemes in more detail. Fig. 9a shows a cylindrical paramagnetic sensor surrounded by a circular loop of wire, which forms the inductance of a SQUID. An additional, non-magnetic absorber for particle detection is assumed to be connected to the top surface of the sensor. The sensor as well as the SQUID are exposed to a homogeneous magnetic field oriented perpendicular to the surface of the substrate. The optimization of signal size and signal-to-SQUID-noise of this configuration will be discussed in detail in the next section.

Fig. 9b illustrates a configuration in which the SQUID-inductance is split into two counterwound circular loops connected in series, forming a planar gradiometer of first order. Each of the loops is filled with a cylindrical sensor. Again, sensor and SQUID are exposed to a homogeneous external field. Depositions of energy in the left and in the right sensor produce changes of flux in the SQUID of opposite sign and can therefore be distinguished. The advantages of this setup are a reduced sensitivity to fluctuations of external fields and a reduced sensitivity to fluctuations of the temperature of the substrate, which may be caused by energetic particles being stopped in adjacent sensors of an array or by a fluctuating power dissipation in the SQUID readout. Moreover, in an array of detectors, the number of wires can be reduced by a factor of two. One disadvantage of this configuration is that the intrinsic noise of two detectors is summed in one electronic channel. Also, the inductance of the pickup loop, which is the SQUID in this case, is increased by a factor of two, leading to a $\sqrt{2}$ times larger flux noise. Both penalties together result in the ultimate energy resolution of this detector being larger by a factor of $\sqrt{2}$ compared to the energy resolution of a single pixel detector.

Fig. 9c is a schematic diagram of a cylindrical sensor with wire-wound pickup coil, which is transformer coupled to a dc-SQUID. As discussed above, in this configuration one pays the penalty of increased energy noise referred to

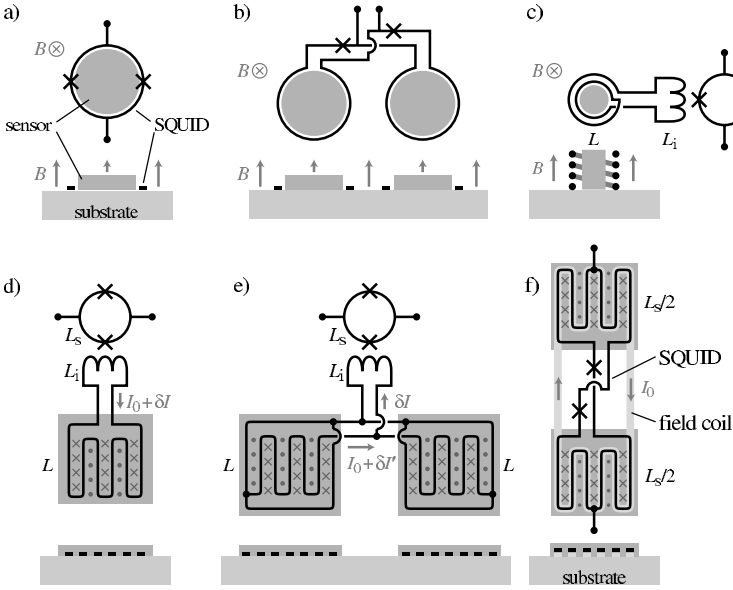

Fig. 9. Several examples of possible coupling schemes to measure the magnetization of paramagnetic sensors with a dc-SQUID. (**a**)–(**c**) assume a homogeneous external magnetic field B. In (**d**) and (**e**) a persistent current I_0 in the meandering superconducting wire of the pickup loop produces an inhomogeneous field in the volume of the sensor. In (**f**) a persistent current I_0 flowing in a closed superconducting loop (*light grey*) underneath the SQUID loop generates an inhomogeneous magnetic field in the volume of the sensor

the pickup coil. On the other hand, the setup permits the spatial and thermal separation of SQUID and sensor. This kind of setup can also be extended to a pickup coil which is split into two counterwound coils connected in series to readout two separate sensors. Benefits and costs of this configuration are similar to those discussed in relation to that of Fig. 9b.

The setup depicted in Fig. 9d differs from the ones discussed so far, as it does not make use of a homogeneous external magnetic field. Instead, a large persistent current I_0 is injected into the superconducting circuit of the flux transformer, *e.g.*, by using a superconducting persistent current switch. The current I_0 produces a strongly inhomogeneous field around the meandering wire of the pickup loop within the volume of the sensor. Upon the deposition of energy δE in the sensor, its magnetic susceptibility decreases by $\delta\chi$, resulting in a change of inductance $\delta L \propto \delta\chi$ of the pickup coil and a change of flux $\delta\Phi_\mathrm{s} = M_\mathrm{is}\delta I \propto \delta\chi \propto \delta E$ in the SQUID. The setup shares all the properties due to transformer coupling that configuration c) possesses. The expected signal-to-noise-ratio of this configuration will be discussed in detail in a subsequent section. It has several advantages. 1. As the bias field for the sensor is produced by the pickup coil itself, even sensor material outside the

area enclosed by the pickup loop can contribute positively to the flux signal in the coil. This sensor/coil configuration has a large filling factor. 2. If very thin sensor films and a very fine pitch of the meander structure are used, one can fabricate sensors of rather large area without a reduction in signal-to-noise ratio. This may be helpful in some applications. 3. The magnetic response of the sensor can no longer be described by a dipolar field, as is the case for in the first three examples. Rather, the field is a multipole of high order, and the magnetic crosstalk in an array of detectors can be reduced significantly. Meander coils are likely to find application in large detectors with thin sensors formed by vapor deposition. In such a geometry it is possible to contemplate placing sensor material on both sides of the plane of the meandering pickup coil, thereby doubling the filling factor. This improves the signal-to-SQUID-noise ratio by $\sqrt{2}$.

Fig. 9e illustrates a setup based on meander-shaped pickup coils to read out two sensors simultaneously. The two meanders together with the input coil of a current-sensor SQUID are connected in parallel to form a flux transformer, where best coupling,

$$\left.\frac{\delta\Phi_\mathrm{s}}{\delta\Phi}\right|_\mathrm{max} = \left.\frac{k\sqrt{L_\mathrm{i}L_\mathrm{s}}}{L+2L_\mathrm{i}}\right|_\mathrm{max} = \frac{1}{2\sqrt{2}}\sqrt{\frac{L_\mathrm{s}}{L}}\,, \tag{23}$$

is achieved if the inductance L_i of the input coil equals half of the inductance L of one meander. An advantage of this configuration is that the rather large current I_0, which is needed to produce the bias field for the sensor, needs not to flow through the input coil of the SQUID. It can be injected into the superconducting loop formed by the two meanders. The input coil and the interconnects between the current-sensor SQUID and the pickup coils only have to carry the small current change δI, which is caused by the deposition of energy in one of the sensors. This configuration has several advantages. 1. The fields are small in the vicinity of the SQUID. 2. There are no special requirements for the critical current of the wires of the input coil. 3. There should be reduced sensitivity to fluctuations of the inductance of the interconnects resulting from vibrations of those wires.

Again, the sign of the flux change in the SQUID can be used to determine which of the two sensors was hit, and the setup is insensitive to temperature fluctuations of the substrate. In addition, note that each of the meanders in configuration e) is enclosed in a square superconducting loop. This gradiometer structure helps to suppress the pickup of alternating external fields and fields caused by Johnson-noise currents within the metallic sensors and absorbers. The idea to use meander-shaped pickup coils being enclosed by a superconducting loop has first been suggested by *Zink* et al. [40] and we shall show some of their results in a later section of this chapter.

Figure 9f is a sketch of a two-pixel detector in which the wires of the meander are the inductive loop of the SQUID. As it is non-trivial problem to have persistent currents flowing in the SQUID inductance, a second superconducting circuit is added to provide the field, whose wiring (light grey) lies

directly underneath the wiring of the SQUID (black). Note that the wires of the SQUID are crossed in the center, in order to form a gradiometer with respect to the field coil. Otherwise flux conservation within the field coil in persistent mode would prohibit flux changes in the SQUID. For the sake of clarity we have omitted enclosing the meanders within a superconducting loop, as illustrated in Fig. 9e. Setup 9f in principle shares all advantages with that of setup 9e. However, due to the absence of a flux transformer one has to expect a stronger thermal coupling between SQUID and sensor, a condition which might be disadvantageous in the context of large detector arrays, as mentioned above. In the case of small detector arrays and meander inductances below 100 pH, the elimination of the factor of 4 loss due to transformer coupling may make this a desirable configuration.

2.4.3 Cylindrical Sensors

The first question to ask is: what best characterizes the performance of an MMC and therefore should be optimized? In an earlier discussion[32], the flux change per unit energy input $\delta\Phi/\delta E$ in the SQUID loop was the parameter that was maximized. This quantity can be written as

$$\frac{\delta\Phi}{\delta E} = \mu_0 \frac{G}{r} \frac{1}{C_\mathrm{s} + C_\mathrm{a}} V \frac{\partial M}{\partial T} . \tag{24}$$

However, what is ultimately of importance is not the size of the signal but the ratio of the size of the signal to that of the noise. In the event that the flux noise were independent of the input coil, then optimizing $\delta\Phi$ would be appropriate. But if the flux noise, $\sqrt{S_\Phi}$, referred to the input coil depends upon the input inductance, as is typically the case, it is the ratio of $\delta\Phi/\delta E$ to $\sqrt{S_\Phi}$, which should be optimized.

To take a specific example, we assume a SQUID whose noise is quantum limited, that is, the noise energy ϵ_s per Hz is some multiple of Planck's constant. Then the flux noise per $\sqrt{\mathrm{Hz}}$ is $\sqrt{S_\Phi} = \sqrt{2\epsilon_\mathrm{s} L}$, L being the inductance of the loop. For a circular loop the inductance is proportional to the radius, $L = \mu_0 \lambda r$, where the constant λ depends on the geometry of the loop. (For $w = 0.1r$, $\lambda = 3.72$, where, as before, w is the width of the thin loop.)

A comparison of signal to noise involves the question of the time dependence of the signal. Rather than enter into the details of that discussion here, we leave such considerations to the next section and focus on the physical properties of the sensor that lead to the best signal to noise, irrespective of temporal response. Then, the quantity we wish to optimize is

$$\mathcal{S} = \frac{\delta\Phi/\delta E}{\sqrt{L}} = \mu_0 \frac{G}{r} \frac{1}{C_\mathrm{s} + C_\mathrm{a}} V \frac{\partial M}{\partial T} \frac{1}{\sqrt{\mu_0 \lambda r}} , \tag{25}$$

or

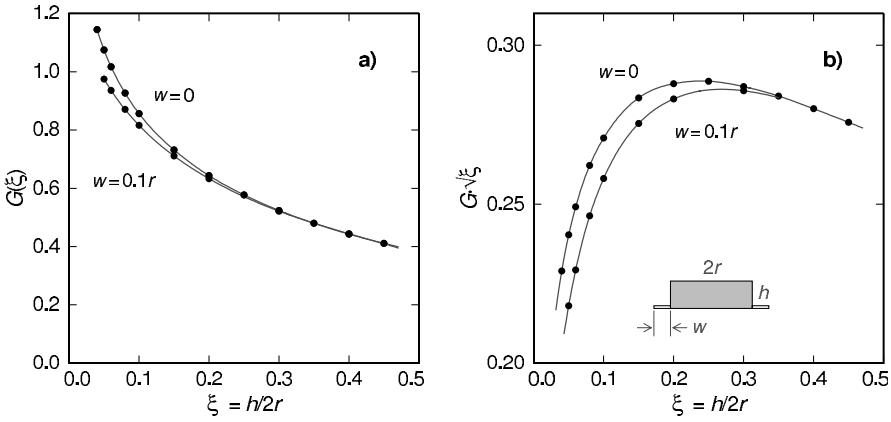

Fig. 10. (**a**) Coupling factor G as a function of reduced sensor height $\xi = h/2r$. (**b**) Product $G\sqrt{\xi}$ to be maximized for optimal signal-to-SQUID-noise ratio

$$\mathcal{S} = \frac{\delta\Phi/\delta E}{\sqrt{L}} = \sqrt{\frac{\mu_0}{\lambda}}\,\frac{G}{r^{3/2}}\,\frac{V}{Vc + C_\mathrm{a}}\,\frac{\partial M}{\partial T}\,. \tag{26}$$

with c being the heat capacity of the spins per unit volume. The quantity $\mathcal{S}$ is of little physical significance except insofar as its optimization is relevant for maximizing the signal to noise when the noise is dependent on inductance. It depends upon a number of parameters.

$$\mathcal{S} = \mathcal{S}(C_\mathrm{a}, g, \alpha, T, x, r, h, B)\,. \tag{27}$$

Four parameters – the heat capacity of the absorber C_a, the g-factor of the paramagnetic ions, the strength of the RKKY interaction α, and the operating temperature T – are generally fixed by the experimental conditions and choice of materials. However, the other four – the concentration of ions x, the radius r and height h of the cylindrically shaped sensor, and the applied magnetic field B – are adjustable. The values of these latter four parameters can be varied so as to maximize $\mathcal{S}$.

First consider r and h, and replace h using $\xi = h/2r$ and write $G/r^{3/2} = \sqrt{2\pi\xi/V}\,G$. Then

$$\mathcal{S} = \sqrt{\frac{\mu_0}{\lambda}}\,\sqrt{2\pi\xi}\,G\,\frac{\sqrt{V}}{Vc + C_\mathrm{a}}\,\frac{\partial M}{\partial T}\,. \tag{28}$$

The coupling factor, G, is independent of volume and is a function of ξ only. Figure 10 shows the coupling factor G as well as the product $G\sqrt{\xi}$ as a function of ξ for two different widths of the pickup loop. For $w = 0.1r$, the product $G\sqrt{\xi}$ has a maximum at $\xi = 0.268$ or $h \approx 0.54r$, $[G\sqrt{\xi}]_\mathrm{max} = 0.286$.

The volume dependence of $\mathcal{S}$ is contained in the factor $\sqrt{V}/(Vc + C_\mathrm{a})$, which leads to the condition $Vc = C_\mathrm{a}$, namely, the heat capacity of the sensor

should equal the heat capacity of the absorber for maximum signal-to-noise. When V is replaced by C_a/c, the optimized $\mathcal{S}$ becomes

$$\mathcal{S}_\mathrm{opt} = \sqrt{\frac{\mu_0}{\lambda}}\; G\sqrt{\frac{\pi\xi}{2}}\;\frac{1}{\sqrt{C_\mathrm{a}}}\;\frac{1}{\sqrt{c}}\frac{\partial M}{\partial T}\bigg|_\mathrm{opt}\,. \tag{29}$$

The last factor, $(1/\sqrt{c})(\partial M/\partial T)$, contains the information on how the concentration and magnetic field should be adjusted to maximize $\mathcal{S}_\mathrm{opt}$ given the values of the fixed parameters, T, g, and α. Because of the spin interactions, a calculation of the optimal conditions can only be performed numerically. However, given the scaling laws obeyed by spins interacting through the RKKY mechanism, as discussed earlier, the functional dependence of x and B on T, g, and α for optimization can be deduced without numerical evaluation. Since all thermodynamic parameters scale as T/x and B/x, the concentration that optimizes S must be proportional to the operating temperature, $x \propto T$. For fixed g, and α, $B_\mathrm{opt}/x_\mathrm{opt}$ = constant so that $B_\mathrm{opt} \propto T$. And since B is always multiplied by g, it follows that $B_\mathrm{opt} \propto 1/g$.

Within the mean field approximation the energy splitting of a spin with $S = 1/2$ is

$$\mathcal{E} = -g\mu_\mathrm{B}(B + xB_i) = g\mu_\mathrm{B}B(1 + xB_i/B)\,, \tag{30}$$

where the dependence on the magnitude of the interactions arises through B_i. Again, because of scaling xB_i/B must be a constant under optimal conditions. Since $B_i \propto g\,\alpha$ it follows that

$$x_\mathrm{opt} \propto T\,g^{-2}\alpha^{-1}\,. \tag{31}$$

The heat capacity of the spins is $c_\mathrm{opt} \propto x_\mathrm{opt}(\mathcal{E}/k_\mathrm{B}T)^2$. Since $\mathcal{E}/(k_\mathrm{B}T)$ is independent of the variables, c_opt has the same dependence on the variables as x_opt.

There is one caveat that one has to append to this discussion. The heat capacity c of the sensor is not simply that of the spins, as has been implicitly assumed to this point, but contains the heat capacity of the conduction electrons[6]. But since the electronic heat capacity, c_e, is proportional to temperature, the dependence of c_opt on T is unchanged by the inclusion of c_e. The same holds true for the temperature dependence of x_opt and $\mathcal{S}_\mathrm{opt}$, discussed below. However, because c_e is unrelated to the spins, the functional dependencies of the optimized parameters on g and α are not strictly valid. Under typical conditions the electronic heat capacity is only a few percent of the spin heat capacity, and there is little error in maintaining the functional form obtained from scaling. In deriving the numerical results below for Au:Er, we have included the electronic heat capacity.

The temperature derivative of the magnetization has the form $\partial M/\partial T \propto x\,g^2\,B\,T^{-2}$. Hence $(\partial M/\partial T)_\mathrm{opt} \propto g^{-1}\alpha^{-1}$, and therefore S_opt has the form

[6] The heat capacity of the lattice is very small and not considered

$$\mathcal{S}_{\rm opt} \;\propto\; (C_{\rm a}\,\alpha\,T)^{-1/2}. \tag{32}$$

The quantities $\sqrt{c}$ and $(\partial M/\partial T)$ have the same dependence on g-value. Hence $\mathcal{S}_{\rm opt}$ is independent of g.

Table 1. The dependence of the variable parameters B, x, r, h, upon the operational parameters $C_{\rm a}$, T, g, and α such that the sensitivity $\mathcal{S} = (\delta\Phi/\delta E)/\sqrt{L}$ is optimized. The *last column* contains explicit values for an Au:Er sensor ($g = 6.8, \alpha = 5$) at 50 mK connected to an absorber that has a heat capacity of $C_{\rm a} = 1 \times 10^{-12}$ J/K

Parameters, that maximize $\mathcal{S} = (\delta\Phi/\delta E)/\sqrt{L}$ for cylindrical sensors				Example: Au:Er, $T = 0.05$ K $C_{\rm a} = 1 \times 10^{-12}$ J/K
$B_{\rm opt}$	=	$2.1\,{\rm T\,K^{-1}}$	$\times\; T g^{-1}$	15 mT
$x_{\rm opt}$	=	$10.3\,{\rm K^{-1}}$	$\times\; T g^{-2}\alpha^{-1}$	2200 ppm
$r_{\rm opt}$	=	$0.64\,{\rm cm}\frac{{\rm K}^{2/3}}{{\rm J}^{1/3}}$	$\times\; (C_{\rm a} g^2 \alpha T^{-1})^{1/3}$	10.7 µm
$h_{\rm opt}$	=	0.53	$\times\; r_{\rm opt}$	5.7 µm
$\mathcal{S}_{\rm opt}$	=	0.093	$\times\; (C_{\rm a}\alpha T)^{-1/2}$	

The results of a numerical calculation of $(1/\sqrt{c})(\partial M/\partial T)$ to obtain the numerical coefficients in the expressions for $x_{\rm opt}$ and $B_{\rm opt}$ are given in Table 1. The dependence on the fixed parameters of $r_{\rm opt}$ and $h_{\rm opt}$, which follow from equating heat capacities, are also given in the table. And finally the optimum signal-to-noise is obtained when

$$\mathcal{S}_{\rm opt} = 0.093\,(C_{\rm a}\alpha T)^{-1/2}\,. \tag{33}$$

The *right column* of Table 1 contains explicit values for $B_{\rm opt}$, $x_{\rm opt}$, $r_{\rm opt}$ and $h_{\rm opt}$ for a specific example. At first glance, the value for the optimal concentration of 2200 ppm may seem somewhat high considering that the calculation assumes the small concentration limit. However, the spin glass transition temperature at this concentrations is still about one order of magnitude lower than the operational temperature $T = 0.05$ K assumed in this example.

In [28] and [32] the quantity that was maximized was the change in flux through a circular loop. In the event that the noise limiting the resolution of the calorimeter is independent of the inductance of the input coil, this is the appropriate quantity to consider. The expression for flux change per unit energy input to the calorimeter is given by (24). The condition that $\delta\Phi$ is a maximum leads to the condition $C_{\rm s} = Vc = 2\,C_{\rm a}$. Again using $\xi = h/2r$, $\delta\Phi_{\rm max}/\delta E$ can be expressed as[7]

$$\left(\frac{\delta\Phi}{\delta E}\right)_{\rm max} = \mu_0 G (2\pi\xi)^{1/3}\;\frac{2^{2/3}}{3}\;\frac{1}{C_{\rm a}^{1/3}}\;\left(\frac{1}{c^{2/3}}\frac{\partial M}{\partial T}\right)_{\rm max}. \tag{34}$$

[7] In this case we use the subscript *max* rather than *opt* for ease in distinguishing the two different optimizations

The results of analyzing the factor containing c and $\partial M/\partial T$ numerically are given in Table 2. The dependences of the optimal values of B, x, and r on the fixed parameters C_a, g, α, and T are the same for $\mathcal{S}_\mathrm{opt}$ and $[\Phi/\delta E]_\mathrm{max}$ but the numerical coefficients are different. The coefficients for r_max and h_max in Table 2 are somewhat different than given in [32] so as to correspond to the configuration of the pickup loop used here of $w = 0.1r$. Also, the numerical factor in $(\delta\Phi/\delta E)_\mathrm{max}$ differs slightly because of a more detailed analysis. We find

$$\left(\frac{\delta\Phi}{\delta E}\right)_\mathrm{max} = 1.3\times10^{-9}\left(\frac{g}{C_\mathrm{a}\alpha T^2}\right)^{1/3}\ \Phi_0/\mathrm{eV}, \tag{35}$$

where $\Phi_0 = 2.07\times10^{-15}\,\mathrm{Vs}$ is the flux quantum.

Table 2. The dependence of the variable parameters B, x, r, h, upon the operational parameters C_a, T, g, and α such that the sensitivity $[\delta\Phi/\delta E]_\mathrm{max}$ is maximized. The last column contains explicit values for an Au:Er sensor ($g = 6.8,\ \alpha = 5$) at 50 mK connected to an absorber that has a heat capacity of $C_\mathrm{a} = 1\times10^{-12}\,\mathrm{J/K}$

Parameters, that maximize $\delta\Phi/\delta E$ for cylindrical sensors		Example: Au:Er, $T = 0.05\,\mathrm{K}$ $C_\mathrm{a} = 1\times10^{-12}\mathrm{J/K}$
$B_\mathrm{max} =$	$1.5\ \mathrm{T\,K^{-1}}\times Tg^{-1}$	11 mT
$x_\mathrm{max} =$	$4.2\ \mathrm{K^{-1}}\times Tg^{-2}\alpha^{-1}$	900 ppm
$r_\mathrm{max} =$	$1.6\ \mathrm{cm}\frac{\mathrm{K}^{2/3}}{\mathrm{J}^{1/3}}\times(C_\mathrm{a}g^2\alpha T^{-1})^{1/3}$	26 µm
$h_\mathrm{max} =$	$0.25\times r_\mathrm{max}$	6.5 µm
$[\delta\Phi/\delta E]_\mathrm{max} =$	$1.3\times10^{-9}\ \frac{\Phi_0}{\mathrm{eV}}\frac{\mathrm{J}^{1/3}}{\mathrm{K}}\times(g\,C_\mathrm{a}^{-1}\alpha^{-1}T^{-2})^{1/3}$	$1.0\times10^{-4}\ \frac{\Phi_0}{\mathrm{eV}}$

Note that $(\delta\Phi/\delta E)_\mathrm{max}$ in (35) has a different dependence on C_a, g, α, and T than does $\mathcal{S}_\mathrm{opt} = [(\delta\Phi/\delta E)/\sqrt{L}]_\mathrm{opt}$ in (33). In particular, $(\delta\Phi/\delta E)_\mathrm{max}$ depends on the g-value of the spins, whereas $\mathcal{S}_\mathrm{opt}$ does not. The difference in functional dependence of these two optimized quantities on the fixed parameters does not carry over to magnetic field, concentration and radius. In both cases the optimal value of field is proportional to T/g, but the constant of proportionality is somewhat larger for the case of $\mathcal{S}_\mathrm{opt}$ than it is for $(\delta\Phi/\delta E)_\mathrm{max}$. The situation is similar for the concentration. This is related to the fact that $\mathcal{S}$ is less sensitive to the heat capacity of the spins than is $\delta\Phi/\delta E$.

The fact that $\mathcal{S}_\mathrm{opt}$ does not depend upon the g-value of the spins does not mean that g is an irrelevant parameter when $(\delta\Phi/\delta E)/\sqrt{L}$ is a measure of the signal to noise[8]. For technical reasons it may be desirable to work

[8] The fact that $\mathcal{S}_\mathrm{opt}$ is independent of g, while $\delta\Phi/\delta E$ is not, is a consequence of the manner in which we chose to describe the exchange interaction in terms of the parameter α so that $B_i \propto x\,g\,\alpha$

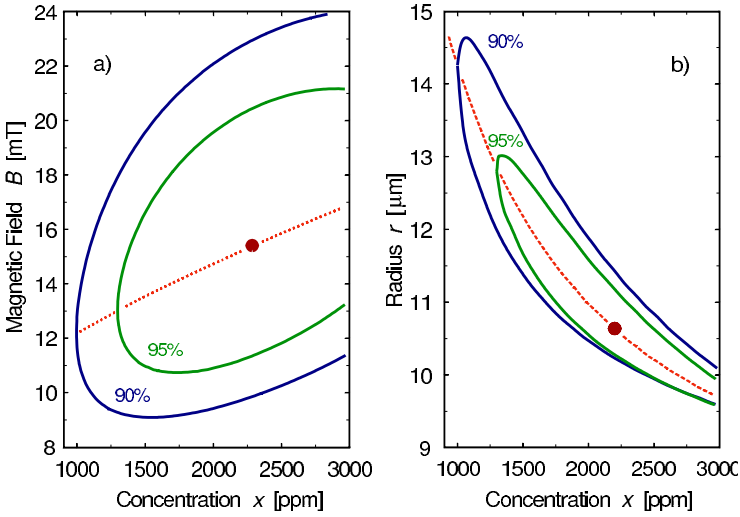

Fig. 11. (**a**) Contours of constant $\mathcal{S} = (\delta\Phi/\delta E)/\sqrt{L}$ in the field/concentration plane for values of S that are 5% and 10% less than $\mathcal{S}_{\rm opt}$ at $T = 0.05$ K, $g = 6.8$ and $\alpha = 5$. The *dotted line* indicates the fields for which $\mathcal{S}$ is a maximum at a given concentration. (**b**) Contours in the radius/concentration plane for the same conditions and $C_{\rm a} = 10^{-12}$ J/K. The *dotted line* indicates the radius of the cylindrical sensor for which $\mathcal{S}$ is a maximum at a given concentration

with as low an applied magnetic field and concentration of spins as possible, conditions which favor a system with high g-value. In this regard, note that $\mathcal{S}$ is not a particularly strong function of the values of the magnetic field and concentration in the vicinity of its maximum. In Fig. 11a we have plotted contours of constant $\mathcal{S}$ at 90% and 95% of $\mathcal{S}_{\rm opt}$ in the field/concentration plane for the conditions $T = 0.05\,\mathrm{K}$, $g = 6.8$ and $\alpha = 5$. The magnetic field can be decreased by a third and concentration by more than a factor of 2 without decreasing the signal to noise by more than 10%. If one adopts a strategy of reducing B and x, then the dimensions of the sensor must be increased to maintain the equality of the heat capacity of the sensor to that of the absorber, as shown in Fig. 11b. In order to achieve a signal to noise of 90% of $S_{\rm opt}$ with the field and concentration reduced to their lowest levels, the radius of the sensor must be increased by about 40%.

2.4.4 Meander Geometry

For many applications, a magnetic calorimeter with a sensor in the form of a small circular cylinder may have technical disadvantages. A large-area pickup loop of meander geometry with a thin sensor and an absorber vapor-deposited on top of it may provide significant improvements in both sensitivity and ease of fabrication. The reason why a meander loop can be made, in principle,

more sensitive than a circular loop is that the spins of the magnetic sensor are on average closer to the pickup loop with the meander geometry. The coupling between spins and pickup loop is larger. Given the fact that the meander-shaped pickup coil is likely to be transformer coupled to a SQUID, the quantity $(\delta\Phi/\delta E)/\sqrt{L}$ is in most cases probably the relevant quantity to optimize. This issue is the topic of the present section.

The discussion here is restricted to a design in which the magnetic field is produced not by an external coil but rather by passing a current though the same meander pattern that is used to measure the change in magnetization of the sensor. Using the same loop for field generation and pickup is a much more important option to consider for a meander with the sensor uniformly distributed above it than for a circular loop enclosing a cylindrical sample within it. The field generated by a current in the meander is highly non-uniform both in magnitude and direction. Directly between two stripes the field is perpendicular to the plane of the meander varying in sign between successive gaps between stripes. Directly above a stripe the field is parallel to the meander plane. But because of reciprocity, a change in magnetization of the spins, aligned locally with the magnetic field, produces a flux change in the meander in proportion to the magnitude of the local field with sign independent of position.

If finite size effects can be neglected, the inductance of a meander-shaped pickup loop can be written as

$$L = \ell\mu_0 \frac{A}{p}\,, \tag{36}$$

where p is the pitch of the meander structure (center-to-center distance of two neighboring conductors) and A is the area covered by the meander. The constant ℓ depends on the relative width of the stripes, w/p, which are assumed to be made of niobium. A plot of ℓ versus the ratio w/p is given in Fig. 12a. These results are obtained from a finite element calculation where the niobium is assumed to be a perfect diamagnet. With $w/p = 0.425$, the value of ℓ is 0.246.

In all following calculations we assume the thickness of the niobium structures to be 0.05 times the pitch (e.g. 500 nm thick for a pitch of $p = 10\,\mu\text{m}$). Also, the meander is covered with an insulating layer having a thickness of $0.025\,p$. This is of relevance in the calculation of field distributions. A schematic cross section of the meander with sensor is illustrated in Fig. 12b.

The magnetic field produced by a current passing through the meander depends strongly on position. The average of the magnitude of the field in a plane parallel to that of the meander drops exponentially with increasing distance between the two planes as illustrated in Fig. 13a. The distribution of fields over a sensor of reduced thickness ξ defined in reference to the pitch by the expression $\xi = h/p$ can be calculated by standard finite-element techniques. With superconducting stripes, the distribution $P(B, \xi, w/p)$ of the magnitude of the field for the particular case $\xi = 0.36$, $w/p = 0.425$ and an

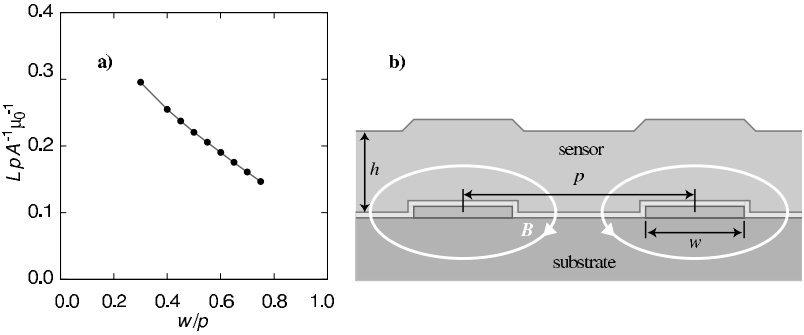

Fig. 12. (**a**) Normalized inductance of a meander shaped coil as a function of the ratio of the width of the superconducting niobium structures w and the pitch p (center-to-center distance of two neighboring niobium stripes). (**b**) Schematic of the cross section of the sensor and the meandering pickup coil wires perpendicular to the current flow. The pitch p, width of the stripes w and height of the sensor h are indicated

average field of $\overline{B} = 12.8\,\mathrm{mT}$ is shown in Fig. 13b. We shall see later that this is the optimal configuration for $g = 6.8$ and $T = 50\,\mathrm{mK}$. The optimal thickness of the sensor, $\xi_{\mathrm{opt}} = 0.36$, turns out to be independent of all other parameters, at least to within 1% of the numerical results.

The quantity G, which is displayed on the top axis of Fig. 13b, has the same meaning as the dimensionless geometrical coupling factor of Sect. 2.4.1. However as used previously, G was an average over the volume of the magnetic sensor whereas here G is a local coupling factor and is a function of the position within the sensor. The equivalent of (17) is, then,

$$\mathrm{d}(\delta\Phi) = \mu_0 \frac{G(\boldsymbol{r}/p)}{p}\,\delta M(\boldsymbol{r})\,\mathrm{d}V\,, \tag{37}$$

where $\mathrm{d}(\delta\Phi)$ is the change of flux in the pickup coil caused by a change of magnetic moment $\delta M(\boldsymbol{r})\,\mathrm{d}V$ in the volume element $\mathrm{d}V$ at position $\boldsymbol{r}$.

As indicated by the use of G in Fig. 13b, this parameter by reciprocity also characterizes the relationship between the magnetic field at a position $\boldsymbol{r}$ and the current I_0 in the meander. The relationship is

$$B(\boldsymbol{r}) = \mu_0 G(\boldsymbol{r}/p)\frac{I_0}{p}\,. \tag{38}$$

Because G depends on the reduced position vector $\boldsymbol{r}/p$, it is independent of the overall dimensions of the meander, but it does depend on the width to pitch ratio w/p of the stripes.

The change of flux $\delta\Phi$ in a meander-shaped pickup coil caused by the deposition of energy δE in the calorimeter can be obtained by placing $\mathrm{d}(\delta\Phi)$ of (37) into (24) and integrating. Since the calorimeter is measured on time

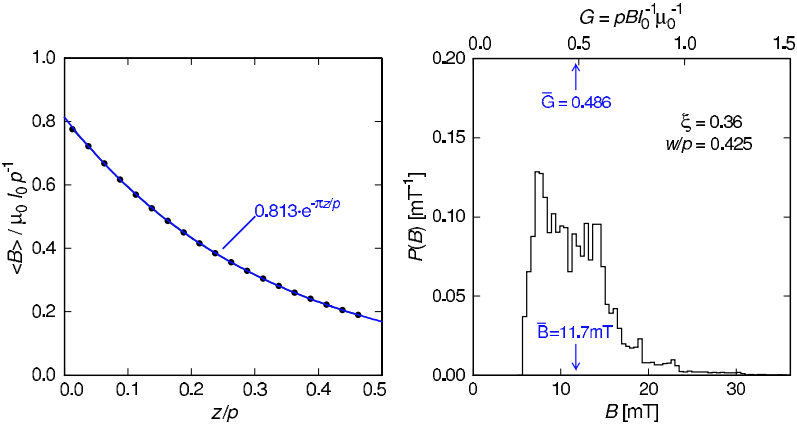

Fig. 13. (**a**) Average magnetic field in a thin layer of sensor material as a function of the distance z between this layer and the surface of the insulating layer, which covers the pickup coil and the meander. The meander has a pitch p and carries a current I_0. (**b**) Distribution of the magnitude of the magnetic field in the volume of a sensor with $\xi = 0.36$. The average field of $\overline{B} = 12.8\,\mathrm{mT}$ corresponds to the optimum field for the operation of a sensor with $g = 6.8$ at a temperature of $T = 50\,\mathrm{mK}$

scales such that it is in thermal equilibrium internally, the temperature rise due to the energy input $\delta T = \delta E / C_{\mathrm{tot}}$ is a constant and can be taken out of the integral. The resulting expression is

$$\delta\Phi = \frac{\delta E}{C_{\mathrm{abs}} + \int_V c(\boldsymbol{r})\,\mathrm{d}^3\boldsymbol{r}} \int_V \mu_0 \frac{G(\boldsymbol{r}/p)}{p} \frac{\partial M[B(\boldsymbol{r}), T]}{\partial T}\,\mathrm{d}^3 r\,, \tag{39}$$

where c is the specific heat per unit volume of the sensor material. The integration of the position-dependent heat capacity of the spins and of $\partial M/\partial T$ can be performed separately.

Since the thermodynamic parameters are functions of field and the distribution $P(B, \xi, w/p)$[9] of magnetic fields within the sensor has already been determined, it is more convenient to integrate over magnetic fields, or rather G, instead of volume. Defining the average value of $\mathcal{X}$ as

$$\langle \mathcal{X} \rangle = \int P(G, \xi, w/p)\, \mathcal{X}\, \mathrm{d}G\,, \tag{40}$$

the expression for $\delta\Phi/\delta E$ becomes

$$\frac{\delta\Phi}{\delta E} = \frac{V}{C_{\mathrm{a}} + V\langle c \rangle} \left\langle \mu_0 \frac{G}{p} \frac{\partial M}{\partial T} \right\rangle . \tag{41}$$

[9] We explicitly note the dependence on w as well as ξ

As with the cylindrical sensor, the quantity we wish to maximize is $\mathcal{S} = (\delta\Phi/\delta E)/\sqrt{L}$. With L given by (36) and the volume of the sensor expressed as $V = A\,h$, $\mathcal{S}$ is

$$\mathcal{S} = \sqrt{\frac{\mu_0}{\ell}}\,\frac{h\sqrt{A/p}}{C_\mathrm{a} + A\,h\,\langle c\rangle}\left\langle G\,\frac{\partial M}{\partial T}\right\rangle . \tag{42}$$

The quantity $\mathcal{S}$ for a calorimeter employing a meander geometry is a function, with some modifications, of the same parameters as for the case of a cylindrical calorimeter. The parameters C_a, g, α, T, and x are obviously the same in the two cases. The field is changed from B to $\overline{B}$, which is replaced in the equations by the experimentally measurable I_0. In place of r we now have the area A of the meander, and h, characterized by the reduced height ξ is now h/p. What is different in the present discussion is the addition of the parameter w/p. The response of a meander is more sensitive to the width of the niobium stripes than is the response in the case of a circular loop, in the optimizing the response of which w was taken as a constant. Altogether $\mathcal{S}$ depends on nine parameters

$$\mathcal{S} = \mathcal{S}(C_\mathrm{a}, g, \alpha, T, x, \overline{B}, A, \xi, w/p)\ . \tag{43}$$

As before, we consider the first four of these parameters fixed by the material and operating conditions and discuss the values of the remaining parameters that produce the maximum value of $\mathcal{S}$.

Equation (42) has a form similar to that of (28). The condition on the volume (or heat capacity) of the spins, which maximizes $\mathcal{S}$, is that $V\langle c\rangle = C_\mathrm{a}$. As a condition on A this is

$$A_\mathrm{opt} = \frac{C_\mathrm{a}}{h\,\langle c\rangle}\ . \tag{44}$$

With this result, the optimized value of $\mathcal{S}$ can be written as

$$\mathcal{S}_\mathrm{opt} = \frac{1}{2}\sqrt{\frac{\mu_0}{\ell}}\,\frac{1}{\sqrt{C_\mathrm{a}}}\sqrt{\frac{\xi}{\langle c\rangle}}\left\langle G\,\frac{\partial M}{\partial T}\right\rangle . \tag{45}$$

The optimal values of the geometrical factors – the ratio w/p and the thickness of the sensor, characterized by $\xi = h/p$ – are independent of the materials parameters and operating temperature. We find that the maximum value of $\mathcal{S}$ is obtained for $\xi_\mathrm{opt} = 0.36$ and $(w/p)_\mathrm{opt} = 0.425$. These quantities are principally defined by the current distribution around the meander stripes. It is interesting to note that the filling factor defined as the ratio of the integral of B^2 over the volume of the sensor to the integral of B^2 over all space,

$$F(\xi, w/p) = \frac{\int_V B^2\,\mathrm{d}^3r}{\int B^2\,\mathrm{d}^3r}\ , \tag{46}$$

Table 3. The dependence of the variable parameters $\overline{B}$, x, A, h for a meander geometry upon the operational parameters C_a, T, g, and α such that the sensitivity $\mathcal{S}$ is optimized. Values for I_opt, $\langle c\rangle_\mathrm{opt}$ and $\langle G(\partial M/\partial T)\rangle_\mathrm{opt}$ are also included to facilitate computations. The *last column* contains explicit values for an Au:Er sensor ($g = 6.8, \alpha = 5$) at 50 mK and $p = 10\,\mu$m connected to an absorber that has a heat capacity of $C_\mathrm{a} = 1 \times 10^{-12}$ J/K

Parameters that maximize $\mathcal{S} = (\delta\Phi/\delta E)/\sqrt{L}$ for planar sensors with meander shaped pickup coil		Example: Au:Er, $T = 0.05$ K $p = 10\,\mu$m, $C_\mathrm{a} = 1$ pJ/K
$\overline{B}_\mathrm{opt} =$	$1.8\,\mathrm{T\,K^{-1}} \times Tg^{-1}$	13 mT
$I_\mathrm{opt} =$	$2.9 \times 10^6\,\mathrm{A\,m^{-1}K^{-1}} \times Tg^{-1}p$	0.21 A
$x_\mathrm{opt} =$	$9.2\,\mathrm{K^{-1}} \times Tg^{-2}\alpha^{-1}$	2000 ppm
$\langle c\rangle_\mathrm{opt} =$	$1.8 \times 10^6\,\mathrm{J\,m^{-3}K^{-2}} \times Tg^{-2}\alpha^{-1}$	$390\,\mathrm{J\,m^{-3}K^{-1}}$
$\langle G\frac{\partial M}{\partial T}\rangle_\mathrm{opt} =$	$2.8 \times 10^5\ \mathrm{Am^{-1}K^{-1}} \times g^{-1}\alpha^{-1}$	$8.1 \times 10^3\,\mathrm{A\,m^{-1}K^{-1}}$
$A_\mathrm{opt} =$	$1.5 \times 10^{-6}\,\mathrm{m^3K^2J^{-1}} \times C_\mathrm{a}g^2\alpha T^{-1}p^{-1}$	$700\,\mu\mathrm{m}^2$
$h_\mathrm{opt} =$	$0.36 \times p$	$3.6\,\mu$m
$L_\mathrm{opt} =$	$4.7 \times 10^{-13}\,\mathrm{H\,m^2K^2J^{-1}} \times C_\mathrm{a}g^2\alpha T^{-1}p^{-2}$	22 pH
$\mathcal{S}_\mathrm{opt} =$	$0.14 \times (C_\mathrm{a}\alpha T)^{-1/2}$	$0.1\,\Phi_0\,\mathrm{keV^{-1}}L_\mathrm{opt}^{-1/2}$

has the value of $F \simeq 0.39$. This is close to the maximum achievable value of 0.50 for a sensor on only one side of the meander.

Because of scaling, the functional dependence of x_opt, $\overline{B}_\mathrm{opt}$, and $\mathcal{S}_\mathrm{opt}$ on C_a, g, α, and T must be the same for the meander geometry as for the cylindrically shaped sensor, i.e., $x_\mathrm{opt} \propto Tg^{-2}\alpha^{-1}$ etc. The results of numerical calculations using the mean field approximation as well as using the diagonalization of the Hamiltonian for clusters of interacting spins, as discussed in Sect. 2.2.1, confirm this result. The coefficients expressing the dependence of the independent parameters that maximize $\mathcal{S}$ on those that are considered fixed are shown in Table 3. The numerical results for the different methods of accounting for the exchange interaction among spins – mean field approximation and the diagonalization of the Hamiltonian of spin clusters – differ for most parameters by less than 5% except in the case of $\overline{B}_\mathrm{opt}$ where the spread is close to 20%. The relations in Table 3 represent a reasonable average of the results of the different numerical methods. In addition, we list in the table several other quantities that are of interest for calculations.

As was the case for a cylindrical sensor, the dependence of $\mathcal{S}$ near its maximum is not a strong function of concentration and field. We have plotted in Fig. 14a contours of constant $\mathcal{S}$ at 95% and 90% of $\mathcal{S}_\mathrm{opt}$ in the field/concentration plane for the conditions indicated in the caption. Also plotted is the field for which the $\mathcal{S}$ is a maximum as a function of concentration. Even at a concentration of 550 ppm, approximately one fourth of the optimal concentration of 2000 ppm, it is possible to achieve a signal that is 80% of the maximum. The penalty of employing a concentration of less than the optimal value is small provided, of course, the field and area of the

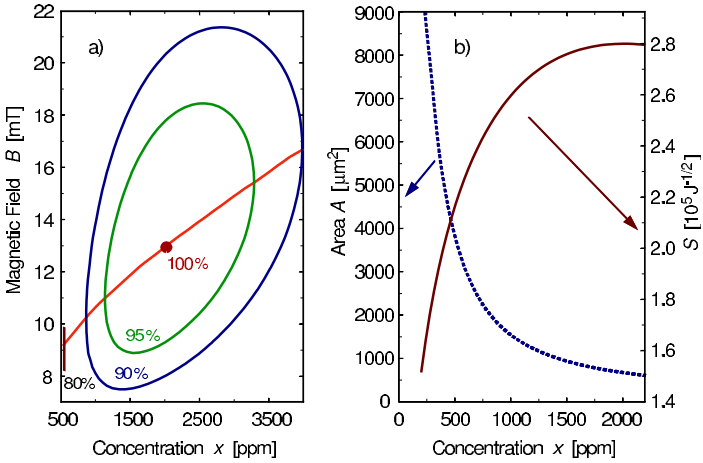

Fig. 14. (**a**) Contours of constant $\mathcal{S}$ at 95% and 90% of $\mathcal{S}_{\rm opt}$ in the field/concentration plane. The *line* indicates the fields for which $\mathcal{S}$ is a maximum at a given concentration. Also indicated is the concentration at which $\mathcal{S} = 0.80\,\mathcal{S}_{\rm opt}$. The parameters associated with the graph are $C_{\rm a} = 1\,{\rm pJ\,K^{-1}}$, $g = 6.8$, $\alpha = 5$, $T = 0.05\,{\rm mK}$ and $p = 10\,\mu{\rm m}$. (**b**) A plot of the maximum value of $\mathcal{S}$ achievable and the area of the meander required to obtain that value as a function a concentration for the conditions in (**a**). The height of the sensor is $3.6\,\mu{\rm m}$

meander can be adjusted accordingly. The maximum value of $\mathcal{S}$ that can be obtained for a particular value of concentration less than the $x_{\rm opt}$ is plotted in Fig. 14b. An empirical equation that fits this curve is

$$\mathcal{S} = \mathcal{S}_{\rm opt}[1 - (240\delta x)^2 - (430\delta x)^6]\,, \tag{47}$$

where $\delta x = (x_{\rm opt} - x)$. This equation fits the calculated values of $\mathcal{S}$ to a few percent for the range $0.2 > \delta x/x_{\rm opt} > 0$. The plot for $\mathcal{S}$ in Fig. 14b and (47) is for the specific values of the parameters $C_{\rm a}$, g, α, and T listed in the caption. The plot and empirical fit is valid for different sets of parameters $C_{\rm a}$ and T, with the replacement of $\mathcal{S}_{\rm opt}$ and $x_{\rm opt}$ by the appropriate scaled values. However, because of the inclusion of the heat capacity of the conduction electrons, the plot and empirical expression are not valid except in the immediate vicinity of $\mathcal{S}_{\rm opt}$, $(\mathcal{S} > 0.95\,\mathcal{S}_{\rm opt})$. As the concentration decreases and the area of the meander increases, as indicated in Fig. 14b, the contribution of the electronic heat capacity becomes an ever larger factor.

The area of the meander required to maximize the signal for a given concentration increases substantially as the concentration decreases, as illustrated by the plot in Fig. 14b. This curve for the area is fit well by the empirical expression

$$A = A_{\rm opt}[1 - (400\delta x) + (800\delta x)^2 - (640\delta x)^8]\,. \tag{48}$$

Again, this equation obeys scaling in T but not in g and α except in the immediate vicinity of the optimal conditions. Also, it should be remembered that all these expressions are derived assuming that finite-size effects are unimportant in computing the fields and inductance. This is certainly not a good approximation, for example, for the optimal conditions in the case illustrated in Fig. 14, where $p = 10\,\mu\text{m}$ and the area covered by the meander-shaped coil is only $A_{\text{opt}} = 700\,\mu\text{m}^2$. But the numbers given in Table 3 and Fig. 14 still provide a useful starting point to derive optimal parameters for meander-shaped pickup coils with smaller pitch or sensors with larger heat capacity and area, where finite size corrections are less important.

The optimization performed above includes many assumptions, such as the volume of the sensor is a variable. There may be situations where this is not the case, for example, the area and thickness of the sensor along the heat capacity of the absorber may be dictated by conditions of the experiment. In such cases the optimal concentration and field could be very different from what is calculated above.

Detectors using a meander pickup may be transformer coupled to a SQUID for best performance. In order to match the meander to the transformer it is essential to have a reasonable estimate of its inductance. In this regard we note that the susceptibility of the sensor under the conditions of optimal signal to noise may be sufficient to warrant its inclusion in the calculation of inductance. For Au:Er at $T = 0.05\,\text{K}$ the optimal concentration is $x_{\text{opt}} = 0.002$, and the susceptibility, using the expressions given in Sect. 2.2.1, is $\chi = 0.18$.

The calculated signal-to-SQUID-noise ratio of MMCs with meander-shaped pickup coil is about 1.5 times better than the result for MMCs with cylindrical sensors in an homogeneous external field. This difference is essentially due to the different filling factors of the two geometries. The fact that we used the meandering wire of the pickup coil to generate the bias field for the sensor allowed for placing sensor material inside as well as outside the area enclosed by the wire of the pickup loop. There might be numerous other sensor/pickup coil geometries with slightly better filling factor and possibly other advantages for certain applications that make use of the same idea.

2.5 Magnetic Johnson Noise

A source of noise, inherent to metallic magnetic calorimeters because of their very nature, is magnetic Johnson noise – noise in the magnetic field or flux, which is generated by thermally induced currents in a conductor. An MMC, consisting of a metallic sensor in close proximity to a pickup loop designed to measure flux changes produced by the sensor, is a system particularly susceptible to the effects of this noise source. Noise can be generated, as well, by a metallic absorber, and other materials in the vicinity of the pickup loop. And while it is noise that must be considered in developing high resolution

MMCs, there are standard means of ameliorating its influence to a degree that it is unlikely to be an important factor in setting limits on performance.

Magnetic Johnson noise has been observed and studied since the development of sensitive SQUIDs. A number of authors [41, 42] have calculated the fluctuations in the magnetic field arising from the thermal currents in a conductor starting from the random motion of the charges. Alternatively, as pointed out by Harding and Zimmerman [43], the flux noise generated in a coil or loop as a consequence of fluctuating currents in a conductor can be calculated using the reciprocity theorem. A time-varying current at frequency ω in a coil produces eddy currents in nearby conductors, and the resulting losses can be described by an apparent resistive impedance $R(\omega)$ of the coil. The impedance can then be used to deduce the flux noise in the coil or loop. This approach was followed in [32] to compute the flux noise in a circular SQUID loop of internal radius r enclosing a cylindrical metallic sensor of the same radius and height h. For this geometry the *rms* flux noise per $\sqrt{\text{Hz}}$ is

$$\sqrt{S_\phi} = \mu_0 \sqrt{\frac{\pi}{8} \mathcal{C}_\text{c} \sigma k_\text{B} T h r^2} \ , \tag{49}$$

where σ is the conductivity of the sensor and $\mathcal{C}_\text{c}$ is a numerical constant that depends on the pickup loop. For the case considered in Sect. 2.4.3 where the width of the loop is $w = 0.1r$, the constant is $\mathcal{C}_\text{c} \approx 2$.

Equation 49 is valid for frequencies such that the dimensions of the sensor are small compared to the skin depth, $\delta = \sqrt{2/(\mu_0 \sigma \omega)}$. It is not possible to write simple analytic expressions for the noise when this condition is not satisfied [41]. The noise drops off rapidly with increasing frequency when the finite skin depth limits the fluctuations from coupling to the loop. In any event, one is unlikely to be concerned about noise in this frequency range, since any change in magnetization of the sensor at these frequencies would be attenuated as well.

The conductivity of $\text{Au}_{1-x}\text{Er}_x$ can be obtained from the work of *Arajs* and *Dunmyre* [31], who found the residual resistivity of this alloy to vary linearly with concentration as $\varrho = x\, 6.7 \times 10^{-6}\,\Omega\,\text{m}$. For a cylindrical Au:Er sensor optimized for the conditions discussed in Sect. 2.4.3, namely, $T = 0.05\,\text{K}$, $C_\text{a} = 1 \times 10^{-12}\,\text{J}\,\text{K}^{-1}$ for which $r_\text{opt} = 10.7\,\mu\text{m}$, $h_\text{opt} = 0.53\,r$ and $x_\text{opt} = 2200\,\text{ppm}$, the magnitude of the magnetic Johnson noise is $\sqrt{S_\phi} \approx 1 \times 10^{-7}\ \Phi_0/\sqrt{\text{Hz}}$.

A metallic absorber attached to the sensor is also a potential source of magnetic Johnson noise. A large conducting sheet of thickness t, parallel to the plane of a circular loop of wire and separated from it by a distance z, produces a spectral flux noise density in the loop of

$$\sqrt{S_\phi} = \mu_0 \pi r^2 \sqrt{\frac{\sigma k_\text{B} T t}{8\pi z(z+t)}} \ . \tag{50}$$

A 5 μm thick absorber with a conductivity of $2 \times 10^8\,\Omega^{-1}\mathrm{m}^{-1}$ (roughly that of vapor-deposited Au) placed 5.7 μm above a 10.7 μm radius loop generates a flux noise of $\sqrt{S_\phi} \approx 2 \times 10^{-7}\,\Phi_0/\sqrt{\mathrm{Hz}}$.

The magnetic Johnson noise can always be reduced by decreasing the conductivity of the metal with non magnetic impurities.

The magnetic Johnson noise for a meander has not been worked out in detail. One can, using numerical methods, calculate the eddy currents losses in the sensor induced by an ac current flowing in the meander strips. This, in turn, can be used to compute the flux noise in the meander generated by fluctuating currents in the sensor. The fluctuating currents principally responsible for producing noise are those that flow parallel to the stripes of the meander. A rough estimate of the contribution of these fluctuations is given by the expression

$$\sqrt{S_\phi} = \mu_0 \sqrt{\mathcal{C}_\mathrm{m} \sigma k_\mathrm{B} T V}\ , \tag{51}$$

where V is the volume of the sensor and $\mathcal{C}_\mathrm{m}$ is a parameter that depends on details of the geometry of the meander. This equation, by itself, is helpful only in showing the obvious dependence on conductivity and temperature. The parameter $\mathcal{C}_\mathrm{m}$ depends on thickness of the sensor. An optimally designed sensor, for which the ratio of thickness to pitch is $\xi = h/p = 0.36$, has a volume which is $V \propto Ap$, where A is the area of the total meander. A rough calculation of $\mathcal{C}_\mathrm{m}$ for an optimal sensor yields $\mathcal{C}_\mathrm{m} \approx 0.02$. Hence, for a meander with a pitch of 10 μm and $A = 1\,\mathrm{mm}^2$ used at 50 mK with a Au:Er sensor having a conductivity of $1.3 \times 10^{-8}\,\mathrm{mho\,m}^{-1}$ (corresponding to an Er concentration of 1000 ppm), the rms flux noise is $\sqrt{S_\phi} \approx 3 \times 10^{-6}\,\Phi_0/\sqrt{\mathrm{Hz}}$. This is an order of magnitude larger than the noise estimated above for a cylindrical sensor and loop, but this is not surprising. The Johnson noise from the sensor in both the cylindrical and meander geometry is proportional to the volume, albeit with a proportionality constant that is different for the two geometries. The volume of the meander sensor chosen in this example is 10^3 times larger than that taken above for the cylinder.

While the fluctuating currents in the sensor flowing parallel to the stripes of the meander are a significant source of magnetic Johnson noise, they are not the only source or even the largest noise source, depending on how the circuit containing the meander is constructed. Consider the three circuits diagrammed in Fig. 15 with the same meander but different configurations of the leads[10]. In the first configuration fluctuating currents in the sensor covering the meander do not couple to the leads. In the latter two configurations where the leads lie very near the sensor there is obvious coupling, but with very different results in the two cases.

[10] Configuration a) is not one that is likely to be used in practice because of the inductance associated with the large area enclosed in bringing the leads together away from the metallic sensor

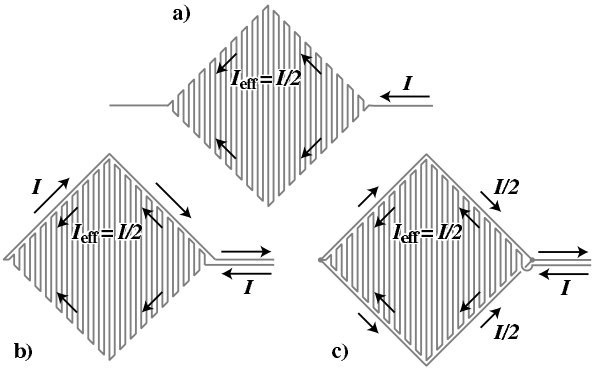

Fig. 15. A meander with three different configurations of the leads connecting it to the remainder of the measuring circuit

In calculating the eddy currents flowing in the sensor to estimate Johnson noise by reciprocity, we need to consider the net current at the boundaries of the meander and not just the current in the stripes. In configuration a) one can approximate the effective current on each side of the meander as $I/2$, I being the total current flowing in the meander. The currents in the upper and lower boundaries flow in the same direction with the result that eddy currents induced in the sensor tend to cancel except in the vicinity of the edges. There is, nonetheless, a contribution to the Johnson noise from fluctuating currents near the edges, but it is not large. The leads play no role in determining the Johnson noise in configuration a).

The same is not true in configuration b), where the return current of I in the lead running along the upper boundary flows in the opposite direction to the effective current of $I/2$ in the meander edge. As a result there is an apparent circumferential current flowing around the meander. A current of $I/2$ flows along the upper and lower boundaries in circular fashion. Time-varying currents in the meander produce large circular eddy currents in the sensor, similar to those in a cylindrical sensor enclosed by a circular loop. The Johnson noise from fluctuating thermal currents is therefore much larger in configuration b) than in a). The noise from fluctuating currents running parallel to the boundaries is estimated to be comparable in magnitude to that produced by currents flowing parallel to the stripes.

The large enhancement of Johnson noise resulting from dressing the lead to lie along the one-half of the meander boundary as in configuration b) can be eliminated by doubling the lead, running one part along the boundary of the upper half of the meander and the other part along the lower half. This is illustrated in configuration c) of Fig. 15. Provided the two halves are symmetric and the current flow is the same in the two parts of the split lead, there is no net current flow around the boundary of the meander. Time-varying currents in the meander produce no circulating eddy currents, or,

to turn the argument around, circular fluctuating thermal currents do not induce voltage or flux noise in the circuit.

As this discussion illustrates, the magnetic Johnson noise in a meander depends on the details of the layout of the circuit and its coupling to the sensor. If necessary, the noise in a meander can be reduced by introducing discontinuities (laminations) in the metallic sensor so as to inhibit thermal currents from flowing in directions that couple either to the stripes or to the edges. This can presumably be accomplished without appreciably changing the area of the sensor and hence the signal response.

The flux noise of MMCs with both, cylindrical sensors with circular pickup loop and planar sensors with meander shaped pickup loop, scale as the volume of the sensor. However, as the change of flux in a meander-shaped pickup coil per unit of deposited energy increases with decreasing pitch of the meander (and decreasing thickness of the planar senor), the signal-to-Johnson-noise ratio can be made significantly larger in this geometry.

2.6 Energy Resolution

Generally speaking, the energy resolution of metallic magnetic calorimeters and other near-equilibrium calorimetric low-temperature particle detectors depends on two properties: the time-dependent signal-to-noise ratio and the time-structure of the signal. If we assume the total noise of the detector signal to be stationary, the discussion of energy resolution is most conveniently carried out in the frequency domain, as discussed in detail by D. McCammon in the introductory chapter of this book.

The energy resolution of MMCs can generally be degraded by numerous effects, such as fluctuations of the detector temperature, electromagnetic interference caused by nearby instruments, magnetic cross-talk between the detectors of a detector-array, infra-red photons due to insufficient screening, and so on. When discussing the ultimate energy resolution of MMCs in the remainder of this section we assume that all these external contributions to noise can be suppressed sufficiently by a proper design of the detector and the refrigerator. In this case we are left with the more intrinsic sources of noise of magnetic calorimeters, being the magnetic Johnson noise caused by the thermal motion of electrons in the metallic sensor, the flux noise (or energy sensitivity) of the SQUID-magnetometer and thermal fluctuations of the magnetic moment of the sensor.

In anticipating the results of the following discussion, we make the following points: 1. magnetic Johnson noise is one of potentially limiting sources of noise. Assuming the sensor to be made of Au:Er, we shall see that its contribution is noticeable in the case of cylindrical sensors. In the case of sensors with meander-shaped pickup coils or materials with smaller conductivity the contribution is marginal. 2. In the preceding section we optimized the signal of MMCs with respect to the flux noise referred to the pickup coil. We shall

see later that the flux-noise of the SQUID magnetometer is a small contribution to the energy resolution of a fully optimized MMC. It is worth keeping in mind that the signal-to-SQUID-noise ratio was found to be best if the heat capacity of the absorber equals the heat capacity of the sensor. We shall see that the optimization of energy resolution, limited by thermodynamic fluctuations of energy, will essentially lead to the same optimal relation between heat capacities, justifying the separation of the two optimizations. 3. The following discussion will show that the most fundamental limitation to the energy resolution of MMCs is set by thermodynamic fluctuations of energy between the thermal subsystems of the calorimeter and fluctuations between the calorimeter and the thermal reservoir.

We discuss the influence of thermodynamic energy fluctuations on the energy resolution in two steps, using two simplified thermodynamic models of the detector. The contribution of the other sources of noise to energy resolution will be discussed in a later section of this chapter.

2.6.1 First Approach – A Canonical Ensemble

In our first approach the calorimeter is described by a simple canonical ensemble. We assume that the detector has a heat capacity C, which is coupled to a thermal reservoir of temperature T_0 by a thermal link with conductance G. In addition, we assume that absorbed energy from energetic particles thermalizes instantly and that we are able to measure the energy content of the calorimeter infinitely fast and with infinite precision.

In the absence of incident particles, the energy content of the calorimeter fluctuates around its mean value with a standard deviation of

$$\delta e_{\mathrm{rms}} = \sqrt{k_{\mathrm{B}} C T^2}\,. \tag{52}$$

Due to the finite values of heat capacity and thermal conductance, the spectral power density of energy fluctuations is restricted to frequencies below $f_0 = (2\pi\tau)^{-1}$,

$$S_{\mathrm{e}} = k_{\mathrm{B}} C T^2 \frac{4\tau}{1 + (2\pi f\tau)^2}\,, \tag{53}$$

where $\tau = C/G$ is the characteristic relaxation time of this configuration.

The deposition of an energy E in the calorimeter causes the energy content to increase instantly and relax back to its mean value following

$$\delta e(t > 0) = E\mathrm{e}^{-t/\tau}. \tag{54}$$

The Fourier spectrum of the signal is described by

$$|\tilde{e}|(f) = E\frac{\tau}{\sqrt{1 + (2\pi f\tau)^2}}\,, \tag{55}$$

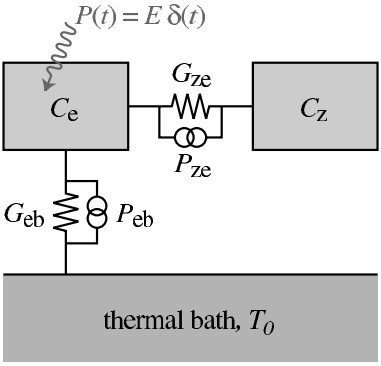

Fig. 16. Thermal model of a magnetic calorimeter consisting of two subsystems, the spins with heat capacity C_z and the conduction electrons of the absorber and the sensor having heat capacity C_e

where $f \in [-\infty, \infty]$. Note that the spectrum of noise and signal have the same dependence on frequency, thus the signal-to-noise ratio is independent of frequency.

When analyzing the data, the information contained in any frequency bin δf can be used to obtain a value for the deposited energy. The uncertainty of the signal in any bin is independent of the center frequency of the frequency interval δf, as long as the width δf is fixed. If the results of N frequency intervals are averaged, the total uncertainty decreases proportionally to $N^{-1/2}$. As the signal-to-noise ratio is independent of frequency, the result of averaging over an infinite number of frequency bins leads to a vanishing uncertainty of the estimated energy.

Of course this result does not reflect the behavior of a real detector. Nonetheless, we learn from this result that the instrumental line width of the detector decreases both by increasing the signal-to-noise ratio in frequency domain and by increasing the usable bandwidth. In a real detector the usable bandwidth can be limited by any of the noise contributions mentioned above. In the following section we show that the thermal fluctuations of energy between the subsystems of the detector already lead to a significant limitation of achievable energy resolution.

2.6.2 Canonical Ensemble Consisting of Two Subsystems

Figure 16 shows a model of a metallic magnetic calorimeter, which consists of two thermal systems, the conduction electrons of the absorber (and the sensor) and the magnetic moments, having heat capacities C_e and C_z, respectively. In order to keep the model as simple as possible, the small contribution of phonons to the total heat capacity is neglected. Moreover, we assume that any deposition of energy E in the detector thermalizes instantly within the system of the conduction electrons. The two systems are connected by a thermal link of conductance G_{ze}. The conduction electrons are connected to a thermal bath of temperature T_0 by a conductance G_{eb}.

In addition, the magnetic moments are assumed to be non-interacting, in the sense that the interaction energy between moments is much smaller than the Zeeman-splitting in the external field. In this case, the total magnetic moment m of the paramagnetic sensor is a measure of the energy content e_z of the spins, being related by $e_\mathrm{z} = -mB$. The magnetic moment, in turn, is proportional to the magnetic flux in the pickup loop, $\delta\Phi \propto \delta m$. Therefore, the flux in the SQUID represents a direct measure of the energy content of the spin system, provided the intrinsic flux noise of the SQUID is neglected.

The time evolution of the energy content of the two systems can be described by the following two differential equations:

$$\dot{e}_\mathrm{z} = C_\mathrm{z}\dot{T}_\mathrm{z} = -(T_\mathrm{z} - T_\mathrm{e})\,G_\mathrm{ze} + P_\mathrm{ze}\,, \tag{56}$$

$$\dot{e}_\mathrm{e} = C_\mathrm{e}\dot{T}_\mathrm{e} = -(T_\mathrm{e} - T_\mathrm{z})\,G_\mathrm{ze} - (T_\mathrm{e} - T_0)\,G_\mathrm{eb} - P_\mathrm{ze} + P_\mathrm{eb} + P(t)\,, \tag{57}$$

where the quantities P_ze and P_zb represent randomly fluctuating fluxes of heat through the thermal links with a white power spectrum of $S_{P_\mathrm{ze}/P_\mathrm{eb}} = 4k_\mathrm{B}T^2G_\mathrm{ze/eb}$. The deposition of an energy E at time t_0 in the detector appears in this set of equation as an external power input $P(t) = E\delta(t - t_0)$ in (57).

Energy Fluctuations.

To derive the power spectrum S_{e_z} of the energy fluctuations of the spins (Zeeman-system), we set $P(t) = 0$ in (57) and transform both equations into the frequency domain. Since both noise sources, P_ze and P_eb, contribute incoherently, the power spectrum is

$$S_{e_\mathrm{z}}(f) = k_\mathrm{B}C_\mathrm{z}T^2\left(\alpha_0\frac{4\tau_0}{1+(2\pi f\tau_0)^2} + \alpha_1\frac{4\tau_1}{1+(2\pi f\tau_1)^2}\right), \tag{58}$$

where $\tau_{0/1}$ represent the characteristic time constants of the system,

$$\tau_{0/1} = \frac{C_\mathrm{e}G_\mathrm{ze} + C_\mathrm{z}(G_\mathrm{ze}+G_\mathrm{eb})}{2G_\mathrm{ze}G_\mathrm{eb}} \mp \sqrt{\frac{[C_\mathrm{e}G_\mathrm{ze} + C_\mathrm{z}(G_\mathrm{ze}+G_\mathrm{eb})]^2}{4G_\mathrm{ze}^2G_\mathrm{eb}^2} - \frac{C_\mathrm{z}C_\mathrm{e}}{G_\mathrm{ze}G_\mathrm{eb}}}\,. \tag{59}$$

The dimensionless factors $\alpha_{0/1}$ are similarly cumbersome functions of C_e, C_z, G_ze and G_eb, which fulfill the simple relation $\alpha_0 + \alpha_1 = 1$. In situations relevant for the following discussion, we take $0.1 < C_\mathrm{z}/C_\mathrm{e} < 10$, $\tau_0 \ll \tau_1$ and approximate $\alpha_{0/1}$ by

$$\alpha_0 = 1 - \beta\,, \tag{60}$$

$$\alpha_1 = \beta\,, \tag{61}$$

where

$$\beta = \frac{C_\mathrm{z}}{C_\mathrm{e} + C_\mathrm{z}} \tag{62}$$

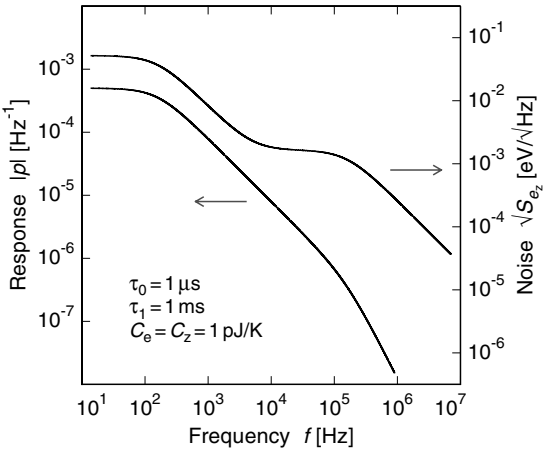

Fig. 17. Frequency spectrum of the response of a MMC (*left axis*) and spectral power density of the energy fluctuations of a MMC. The values correspond to a detector with $C_\mathrm{e} = C_\mathrm{z} = 1\,\mathrm{pJ/K}$, $\tau_0 = 1\,\mu\mathrm{s}$, $\tau_1 = 1\,\mathrm{ms}$ at a temperature of $T = 50\,\mathrm{mK}$

is the relative contribution of the heat capacity of the spins to the total heat capacity of the calorimeter.

Figure 17 shows the frequency spectrum of energy fluctuations of the spin system for a detector having heat capacities $C_\mathrm{e} = C_\mathrm{z} = 1\,\mathrm{pJ/K}$ and time constants $\tau_0 = 1\,\mu\mathrm{s}$, $\tau_1 = 1\,\mathrm{ms}$ at a temperature of $T = 50\,\mathrm{mK}$.

The spectrum is the incoherent sum of two step-like contributions. Fluctuations between the spins and the absorber cause a plateau of amplitude $\sqrt{S_{e_z}} = \sqrt{4k_\mathrm{B}C_\mathrm{z}T^2\tau_0(1-\beta)}$ at high frequencies. Energy fluctuations between the spins and the thermal bath contribute $\sqrt{S_{e_z}} = \sqrt{4k_\mathrm{B}C_\mathrm{z}T^2\tau_1\beta}$ to the spectrum at frequencies below $(2\pi\tau_1)^{-1}$. As expected, the integral of S_{e_z} gives

$$\int_0^\infty S_{e_z}\,\mathrm{d}f = k_\mathrm{B}C_\mathrm{z}T^2\,, \tag{63}$$

which corresponds to the energy fluctuations of a canonical ensemble of heat capacity C_z at temperature T.

Response.

In order to calculate the response $e_\mathrm{z}(t)$ of the detector upon the deposition of energy E, we neglect the random noise sources P_ze and P_eb in (56) and (57) and obtain

$$\frac{e_\mathrm{z}(t>0)}{E} = p\,(t>0) \simeq \beta(\mathrm{e}^{-t/\tau_1} - \mathrm{e}^{-t/\tau_0})\,. \tag{64}$$

The energy content of the spins rises, approaches a maximum value with a time constant τ_0 and relaxes back to its equilibrium value with a time constant τ_1. The responsivity p of the detector is best described in frequency domain by

$$|\tilde{p}|(f) \simeq \frac{\beta\tau_1}{\sqrt{1+(2\pi f\tau_0)^2}\sqrt{1+(2\pi f\tau_1)^2}}\,, \tag{65}$$

where $f \in [-\infty, \infty]$. Again, we assumed $\tau_0 \ll \tau_1$. Figure 17 shows the frequency spectrum of the detector response (*left axis*). The response is a maximum at low frequencies, decreases proportional to f^{-1} at frequencies above $f_1 = (2\pi\tau_1)^{-1}$ and twice as fast, $\tilde{p} \propto f^{-2}$, at frequencies beyond $f_0 = (2\pi\tau_0)^{-1}$. From Fig. 17 it is apparent that the signal-to-noise ratio cannot be improved by summing over an ever increasing frequency range. Hence, the energy resolution is limited to finite values within this model.

The responsivity $\tilde{p}$ as defined in (65) can also be interpreted as the ratio between the amplitude of oscillations of energy content e_z of the spin system and the amplitude of a harmonic power input P into the electron system of the detector. It is therefore straight forward to define the noise-equivalent power NEP by $\mathrm{NEP}^2 = S_{e_z}/(\tilde{p}^*\tilde{p})$. Using the results from above

$$\mathrm{NEP}^2(f) = \mathrm{NEP}_0^2\left[1+(f/f_{\mathrm{eff}})^2\right] \tag{66}$$

with a constant minimum value of

$$\mathrm{NEP}_0^2 \;=\; 4k_{\mathrm{B}}T^2G_{\mathrm{eb}}\left(1+\frac{G_{\mathrm{eb}}}{G_{\mathrm{ze}}}\right) \;\simeq\; \frac{4k_{\mathrm{B}}C_{\mathrm{z}}T^2}{\beta\tau_1} \tag{67}$$

up to a frequency of

$$f_{\mathrm{eff}} = \frac{1}{2\pi C_{\mathrm{e}}}\sqrt{G_{\mathrm{ze}}G_{\mathrm{eb}}\left(1+\frac{G_{\mathrm{eb}}}{G_{\mathrm{ze}}}\right)} \;\simeq\; \sqrt{f_0 f_1}\sqrt{\frac{\beta}{1-\beta}}\,. \tag{68}$$

Again, the approximations are applicable in the case of $\tau_0 \ll \tau_1$. The effectively usable bandwidth of the detector signal is limited to frequencies below f_{eff}, because the noise-equivalent-power increases as $\mathrm{NEP} \propto f$ at frequencies beyond this.

Energy Resolution.

The energy resolution of thermal detectors with frequency-dependent noise-equivalent power was discussed in detail by D. McCammon in the introductory chapter of this book. Within the framework of optimal filtering it was shown that the energy resolution of a detector is related to $\mathrm{NEP}(f)$ by

$$\Delta E_{\mathrm{rms}} = \left(\int_0^\infty \frac{4\,\mathrm{d}f}{\mathrm{NEP}^2}\right)^{-1/2}. \tag{69}$$

When applied to the present model of thermal fluctuations between the subsystems of the detector and to the thermal bath the result is

$$\Delta E_{\mathrm{rms}} = \sqrt{4k_{\mathrm{B}}C_{\mathrm{e}}T^2}\left[\frac{G_{\mathrm{eb}}}{G_{\mathrm{ze}}} + \left(\frac{G_{\mathrm{eb}}}{G_{\mathrm{ze}}}\right)^2\right]^{1/4} . \tag{70}$$

Note that ΔE increases linearly with temperature and square root of absorber heat capacity. However, this expression implies that the energy resolution can be improved without limit if there is a perfect thermal conductance G_{ze} between the absorber (electrons) and the thermometer (spins). But for a given sensor material, e.g. Au:Er, the thermal conductance between electrons and spins is not a freely adjustable parameter. The limiting material parameter is the electron-spin relaxation time, which obeys the Korringa relation $\tau_{\mathrm{K}}T = \kappa$ in the limit of small spin concentrations. For this reason we rewrite (70) in terms of relaxation times and obtain

$$\Delta E_{\mathrm{rms}} = \sqrt{4k_{\mathrm{B}}C_{\mathrm{e}}T^2}\left(\frac{1}{\beta(1-\beta)}\frac{\tau_0}{\tau_1}\right)^{1/4} . \tag{71}$$

Given that the signal rise time τ_0 is fixed by the sensor material and the recovery time τ_1, C_{e} and T are determined by the requirements of a given application, there is only one free parameter, β, that can be used to optimize the energy resolution of the detector. The energy resolution ΔE_{rms} is a minimum for $\beta = 1/2$, meaning that the heat capacity of the spins should match the heat capacity of the absorber. This is consistent with the result of the optimized signal-to-SQUID-noise. Within these assumptions, the intrinsic energy resolution of a magnetic calorimeter can be expressed as [44]

$$\Delta E_{\mathrm{rms}} = \sqrt{4k_{\mathrm{B}}C_{\mathrm{e}}T^2}\sqrt{2}\left(\frac{\tau_0}{\tau_1}\right)^{1/4} . \tag{72}$$

There are a number of comments that may help putting this result into perspective.

1. Due to its very nature, an MMC, being a thermal detector with finite relaxation time for internal equilibration, has an energy resolution that is intrinsically limited. This is true even though, in the model discussed here, the amplifier is assumed to be infinitely fast and noiseless.

2. As the power dissipation to read out the sensors can be made almost arbitrarily small – at least in comparison to resistive temperature sensors – in some applications it may be possible to improve the energy resolution in the limit of long recovery times τ_1, albeit at the expense of a significant limitation to count rate. If an MMC could be used together with a fast heat switch it might be possible to combine the benefits of a long thermal relaxation time τ_1 with high count rates. The transient signal upon the deposition of energy could be analyzed at high signal-to-noise and then afterwards the detector

could be returned rapidly to thermal equilibrium. A similar reduction of the effective thermal recovery time could be achieved by electro-thermal feedback, where the temperature of the calorimeter is elevated above bath temperature by a heater current through the sensor, which is reduced upon the deposition of energy in the detector.

3. The simplified model discussed here does not include the RKKY interaction between the localized magnetic moments. An accurate treatment of the influence of this interaction on energy resolution appears rather complex. A simple argument, which can be used to estimate the order of magnitude of the degradation of resolution, is the following. As discussed above, the magnetic susceptibility of the sensor material can be described by a Curie-Weiss relation $\chi = \lambda/(T + \theta)$. For the material Au:Er $\lambda = x\,5.35\,\mathrm{K}$ and the interaction between the spins is described by $\theta = x\alpha\,1.1\,\mathrm{K}$. Sensors with the best signal-to-SQUID-noise have an erbium concentration of $x_{\mathrm{opt}} \simeq 0.040\,T/\mathrm{K}$. From the Curie-Weiss relation we see that the interaction between the spins reduces the susceptibility of free magnetic ions by about θ/T, which has a value of $\theta_{\mathrm{opt}}/T = 0.22$. Only about 3/4 of the magnetic moments appear to act as non-interacting spins, as assumed in the simplified model. The other 1/4 contribute to the heat capacity of the spin system without contributing to the signal. If we further assume that the relaxation time of this latter system is the order of τ_0, we can conclude that the high frequency plateau of the noise spectrum raised, resulting in a reduction of the effectively usable bandwidth. Within this picture, the effect on energy resolution can be estimated via (71), with the increase of ΔE_{rms} being less than 15%. However, this simple argument does not hold in the limit of high concentrations and low temperatures, where paramagnetic alloys enter the spin glass state and strong spin-spin correlations lead to an increased amplitude of the fluctuations of the magnetic moment. The frequency dependence of the spectral density, $S_{\mathrm{m}} \propto f^{-1}$, is due to a broad distribution of relaxation times. In the examples given above, the sensors are operated at a temperature which is about one order of magnitude higher than the spin-glass temperature of the sensor material, and spin-spin correlations are expected to have a minor effect in this regime.

4. It seems attractive to improve the intrinsic energy resolution of the detectors by choosing a sensor material with a short electron-spin relaxation time. However, due to the underlying physics it is likely that this strategy will also lead to a stronger indirect exchange interaction between the localized magnetic moments, leading to a degradation of energy resolution as discussed above in comment (3.).

5. In our discussion above, we assumed that the signal rise time is determined by the Korringa time τ_{K}. A more detailed discussion should include the fact that electron-spin relaxation time also depends on the ratio of Zeeman splitting $g\mu_{\mathrm{B}}B$ to thermal energy $k_{\mathrm{B}}T$. This leads to an increase of τ_{K} in large magnetic fields. In addition, if the heat capacities of the elec-

tron system and the spins are of similar size, the effective relaxation time is reduced to $\tau_0 = (1-\beta)\tau_\mathrm{K}$. If this relation is inserted into (71) the factor $[\beta^{-1}(1-\beta)^{-1}\tau_0\tau_1^{-1}]^{1/4}$ is replaced by $(\beta^{-1}\tau_\mathrm{K}\tau_1^{-1})^{1/4}$. Now ΔE has a minimum at $\beta = 1$, which is smaller by a factor of $2^{1/4}$ than the value at $\beta = 1/2$. However, this limit is unlikely to be reached in experiments. For fixed C_e the limit $\beta \to 1$ is equivalent to $C_\mathrm{z} \to \infty$, and there is a corresponding increase of energy fluctuations at low frequencies. Theoretically, this increase in noise is compensated by a larger usable bandwidth, since the height of the high frequency plateau of the noise decreases. In practice, there are other effects such as the thermal diffusion time within the absorber that will limit the relaxation time between the absorber and the spins and make considerations of corrections to τ_K mute.

6. The intrinsic limitation of energy resolution, which is discussed in this section, is caused by thermal fluctuations of energy between the absorber and the spins, resulting in a second plateau in the noise spectrum at high frequencies, having an amplitude of $\sqrt{S_{e_\mathrm{z}}} = \sqrt{4k_\mathrm{B}C_\mathrm{z}T^2\tau_0(1-\beta)}$. The spectral power density of flux noise S_Φ in the pickup coil caused by these fluctuations of energy can be estimated from this value by the factors $\delta\Phi/\delta E$ and $(\delta\Phi/\delta E)/\sqrt{L}$, which were derived in the previous sections, resulting in $\sqrt{S_\Phi} \simeq \beta^{-1}\sqrt{S_{e_\mathrm{z}}}\delta\Phi/\delta E$. We shall use this relation to discuss the contribution of magnetic Johnson noise and SQUID noise to the energy resolution of the detector in the following example.

Example.

A microcalorimeter working at a temperature of 50 mK, having an X-ray absorber made of gold with an active area of 240 µm × 240 µm and a thickness of 5 µm might be regarded as a useful detector for high resolution X-ray spectroscopy. The heat capacity of the absorber at this temperature $C_\mathrm{a} = 1.0\,\mathrm{pJ/K}$. In order to obtain an estimate of the intrinsic energy resolution of the calorimeter, we assume relaxation times of $\tau_0 = 1\,\mu\mathrm{s}$ and $\tau_1 = 1\,\mathrm{ms}$. From (72) the energy resolution is $\Delta E_\mathrm{FWHM} = 1.4\,\mathrm{eV}$.

In this example we take the sensor to have cylindrical geometry and to be made of Au:Er with parameters listed in Table 1, which on the one hand correspond to optimum signal-to-SQUID-noise and on the other hand fulfill $C_\mathrm{sensor} = C_\mathrm{a}$, in agreement with the condition $\beta = 1/2$ for optimal intrinsic energy resolution. The sensor has a radius of 10.7 µm, a thickness of 5.7 µm and an erbium concentration of 2200 ppm. It is placed in a field of 15 mT and the circular pickup loop, which is used to read out the sensor, has an inductance of $L = 50\,\mathrm{pH}$. As discussed above, the interaction between the magnetic moments at this concentration will cause the energy resolution of the detector to be degraded by about 15%, leading to $\Delta E_\mathrm{FWHM} \simeq 1.6\,\mathrm{eV}$.

From the values listed in Table 1 and $L = 50\,\mathrm{pH}$ we can derive $\delta\Phi/\delta E = 1.0 \times 10^{-4}\Phi_0/\mathrm{eV}$. Hence, the high frequency plateau of energy fluctuations,

$\sqrt{S_{e_z}} = 1.65 \times 10^{-3}\mathrm{eV}/\sqrt{\mathrm{Hz}}$, corresponds to a flux noise in the pickup coil of $\sqrt{S_\Phi} = 0.33\,\mu\Phi_0/\sqrt{\mathrm{Hz}}$.

This value can now be compared to the flux noise of the SQUID and to flux noise generated by magnetic Johnson noise. Assuming the energy sensitivity of the SQUID to be $\epsilon_\mathrm{s} = 25\hbar$, its contribution to flux noise is $\sqrt{S_\Phi} = 0.25\,\mu\Phi_0/\sqrt{\mathrm{Hz}}$. This reduces the usable bandwidth of the detector signal by 25 % and causes a degradation of energy resolution of 12%, resulting in $\Delta E_\mathrm{FWHM} \simeq 1.8\,\mathrm{eV}$.

The contribution of magnetic Johnson noise of the sensor to the total flux noise was calculated in the preceding section to be $\sqrt{S_\Phi} \simeq 0.1\,\mu\Phi_0/\sqrt{\mathrm{Hz}}$. It also adds incoherently to the magnitude of the high frequency plateau, but its effect on the energy resolution is only the level of 2% and can be neglected.

Since the intrinsic energy resolution for an optimized detector is independent of geometry, a planar sensor with a meander shaped pickup coil would have an almost identical intrinsic energy resolution as a sensor with cylindrical geometry. However, the degradation of the energy resolution by both SQUID noise and magnetic Johnson noise would be somewhat less.

At a given temperature the relative contributions of the three sources of noise to the energy resolution should also hold for detectors that have an absorber heat capacity differing from the example discussed here, because all these contributions scale as $\sqrt{C_\mathrm{a}}$. However, if the detector is operated at lower temperatures, the flux noise of the SQUID becomes increasingly important.

3 Status of Development

Based on the results of a theoretical analysis of signal optimization and of fundamental noise contributions, several prototype detectors have been constructed and tested. Since optimized SQUIDs for MMCs have not yet been fabricated, these prototypes are not fully optimized detectors. They are primarily devices for demonstrating the potential of MMCs for particle detection. In this section we present selected results that have been achieved with these prototype detectors. We focus our discussion mostly on X-ray spectroscopy, one of the main applications for this type of device. In addition, we discuss applications in metrology and gamma-ray detection. At the beginning of this section we briefly mention a few details of the experimental setup for operating magnetic calorimeters.

3.1 Experimental Setup

In the first part of this section we shall describe a cryogenic system that has been used to operate magnetic calorimeters. This should be seen just as an example for a typical cryogenic environment for MMC detectors and serves to illustrate some noteworthy details. In the second part of this section a few important aspects of a suitable SQUID magnetometer setup are discussed.

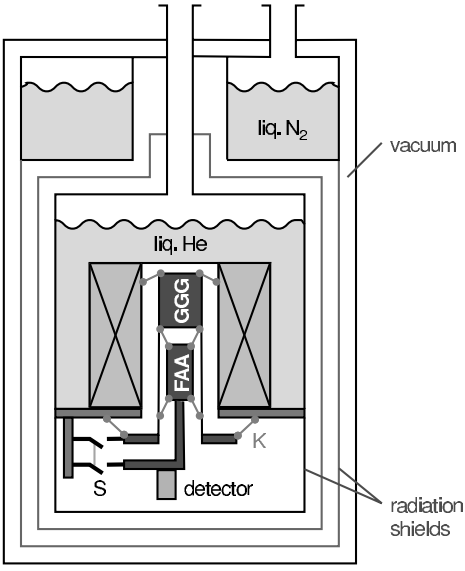

Fig. 18. Schematic of an adiabatic demagnetization refrigerator (ADR)

3.1.1 Cryogenics

The prototypes discussed in the remainder of this chapter were operated in a variety of different cryostats, ^{3}He/^{4}He-dilution refrigerators as well as adiabatic demagnetization refrigerators (ADR). In order provide an idea of the typical cryogenic environment of magnetic calorimeters, we provide a brief description of the cryostat that was used in the experiments on high resolution X-ray spectroscopy discussed in Sect. 3.2.

A sketch of the cryostat is shown in Fig. 18. The commercial 2-stage ADR[11] has a common isolation vacuum, a liquid nitrogen bath and a liquid helium bath. The helium bath provides a platform at a temperature of 4.2 K, which can be lowered to $T = 1.5\,\mathrm{K}$ by pumping. A paramagnetic salt pill (GGG[12]) is suspended from this platform by kevlar strings (K). A second paramagnetic pill (FAA[13]) with lower spin concentration is suspended from the GGG pill also by kevlar strings. Each salt pill has good thermal contact to a separate experimental platform. Both platforms can be thermally connected to the cold platform of the helium bath via mechanical heat switches (S). The salt pills are located in the common vacuum space of the cryostat and surrounded by a superconducting magnet, which is located in the helium bath. Starting the adiabatic demagnetization process of the paramagnetic salt pills at a temperature of $T \simeq 1.5\,\mathrm{K}$ and a field of $B = 6\,\mathrm{T}$ results in base temperatures of $T_{\mathrm{GGG}} \simeq 200\,\mathrm{mK}$ and $T_{\mathrm{FAA}} \simeq 21\,\mathrm{mK}$. After full

[11] VeriCold Technologies GmbH, Ismaning, Germany, www.vericold.com
[12] GGG: Gadolinium-Gallium-Garnet
[13] FAA: Ferric-Ammonium-Alum

demagnetization, the time for the FAA pill to warm up to temperatures above 30 mK is approximately 3 days, providing enough time for long continuous measurements.

The magnetic calorimeters are mounted on the cold platform of the FAA salt pill. All wires running from He-temperature to the detectors are made of material with low thermal conductivity (e.g. NbTi, CuNi) and heat sunk at the GGG-platform. The temperature of the FAA platform is measured using a RuO_2 resistance thermometer with $\mathrm{d}\log R/\mathrm{d}\log T \simeq 1.5$ at $T \simeq 35\,\mathrm{mK}$ and a AVS-47 resistance bridge[14]. A fully analog as well as a digital PID controller were used for regulating the current through the magnetizing coil of the ADR, in order to stabilize the temperature of the FAA platform to within $\delta T_{\mathrm{rms}} \simeq 2\,\mu\mathrm{K}$ in the temperature range between 30 mK and 35 mK.

For MMCs to be used as high resolution X-ray detectors a temperature stability on this level or better is indeed required. The dependence of the detector sensitivity $\delta\Phi/\delta E$ on the operating temperature can be characterized by $\mathrm{d}\log(\delta\Phi/\delta E)/\mathrm{d}\log T \simeq -1$ for MMCs with sensor parameters close to optimum. Therefore, the variations of operating temperature quoted above already contribute $\Delta E_{\mathrm{FWHM}}/E \simeq 1.5 \times 10^{-4}$ to the energy resolution of the detector.

3.1.2 SQUID Magnetometer

Low noise, high bandwidth readout of the SQUID magnetometer of an MMC can be achieved by 2-stage SQUID electronics, as illustrated in Fig. 19. The signal of the primary SQUID (detector SQUID) is amplified by a secondary SQUID (amplifier SQUID) before it is read out by an amplifier operating at room temperature. In order to achieve a high transfer coefficient $\delta U_2/\delta\Phi_1$ of flux Φ_1 in the primary SQUID to voltage U_2 across the secondary SQUID, a dc flux is applied to the secondary SQUID to make the steepest points of the U-Φ-characteristics of the two single SQUIDs fall on top of each other.

Figure 20 shows the U_2-Φ_1-characteristics of the 2-stage SQUID configuration, which was used for the high resolution X-ray detector discussed in Sect. 3.2. The steepest point of the common characteristics is marked with a dot. Linearization of the flux-voltage characteristics is achieved by applying negative feedback to the flux in the primary SQUID and stabilizing the system at the steepest point (working point) of the common characteristics.

The flux-to-flux gain G_Φ between the two SQUIDs at the working point can be adjusted by the resistor R_{g}. To allow for stable operation and to avoid multiple working points, the maximum flux swing in the secondary SQUID caused by the voltage swing of the primary SQUID should not exceed one flux quantum Φ_0. This limits the flux gain to values of about $G_\Phi < 3$.

One major benefit of the 2-stage configuration is the fact that a SQUID with a high critical current and large voltage swing (or even a series-SQUID-

[14] Pico-Watt Electronica, Finland

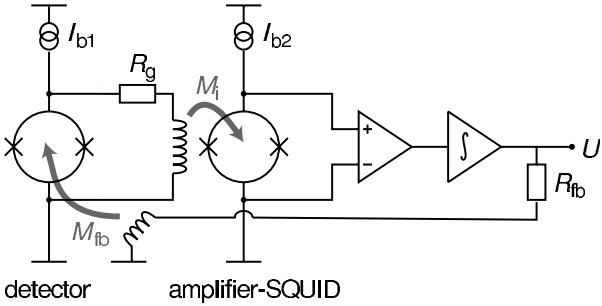

Fig. 19. Schematic circuit diagram of a two-stage SQUID-magnetometer

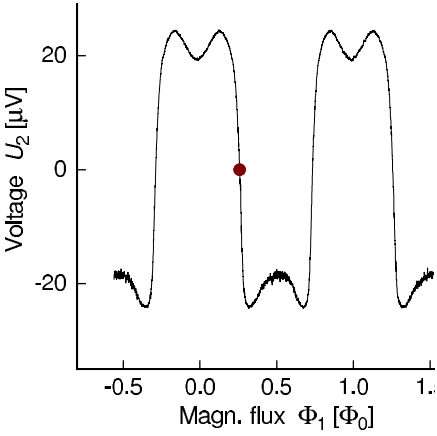

Fig. 20. Flux–voltage characteristics of a 2-stage SQUID configuration. The flux gain at the working point is $G_\Phi \simeq 2.7$

array impedance matched to the room temperature electronics) can be used as the amplifier. On the other hand, the critical current and voltage swing of the detector SQUID can be small without degradation of the noise performance. A dissipated power in the detector SQUID in the range of (10 pW to 100 pW) is desirable in many setups since the thermal bath of the calorimeter is often provided by the SQUID chip itself.

3.2 High Resolution X-ray Spectroscopy

The prototype X-ray detectors discussed in this section are based on commercially available SQUID chips [45], which are designed as first-order gradiometers having two planar loops of 50 μm diameter wound in opposition. To turn these SQUID susceptometers into magnetic calorimeters small discs of Au:Er (diameter 50 μm, thickness 25 μm, containing 300 ppm of isotopically enriched ^{166}Er) are placed by hand into each loop of the gradiometer. The

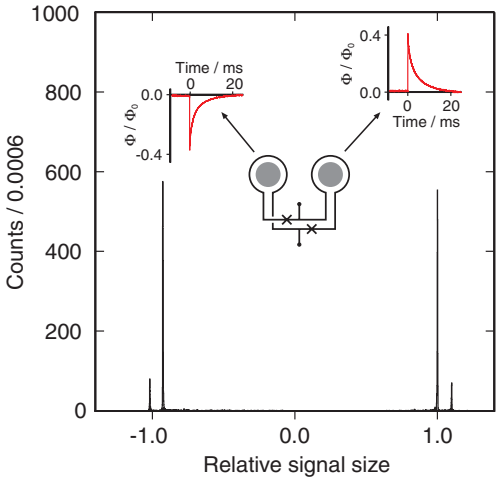

Fig. 21. Response of a two-pixel magnetic calorimeter with single stage SQUID readout. The *insert* is a schematic of the setup of the SQUID gradiometer with an Au:Er sensor in both loops. In addition, a single pulse from each detector pixel is shown. Also, a pulse height distribution is shown that was obtained with the two-pixel detector using a ^{55}Fe source [46]

Au:Er discs are attached with a thin layer of vacuum grease to the substrate and serve in the following experiment as both paramagnetic sensor and X-ray absorber, having a quantum efficiency of effectively 100% at 6 keV.

In this gradiometer configuration fluctuations in the magnetization due to variations of the temperature of the SQUID chip are canceled. In addition, the sensor, or in other experiments the sensor/absorber combination, in each loop is a separate pixel that is read out by the same SQUID. Depending on which pixel is hit by a X-ray, a negative or a positive flux change is registered. Fig. 21 shows the resulting flux change of single 5.9 keV events into each of the two pixels along with a sketch of the gradiometer. The signal size and the thermalization time were the same for both pixels to within 10%. The detector was operated at 25 mK in a field of 2 mT. The thermalization time was roughly 10 ms due to the very weak thermal link between the sensor and the substrate via the vacuum grease. The pulse height spectrum obtained with this device using a ^{55}Fe source is shown in the lower part of Fig. 21. The K_α and K_β lines of ^{55}Mn are clearly seen by both pixels. The pulse heights are plotted on a relative scale normalized to the K_α line measured with positive flux change. The count rates of the two pixels were slightly different, because of a small difference in the collimator masks. The energy resolution at 6 keV is almost identical for the two pixels, being about 9 eV. The slight difference in resolution observed in this experiment originated from the small difference in the signal size of the two pixels.

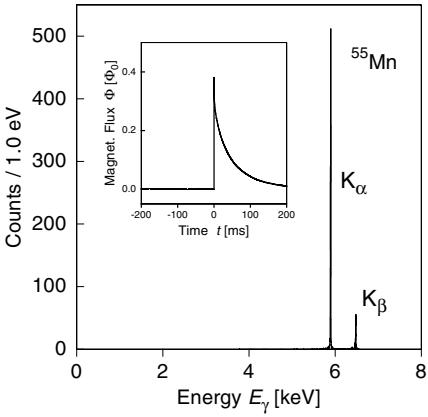

Fig. 22. X-ray spectrum of ^{55}Mn. The *insert* shows the flux change caused by a single 5.9 keV X-ray [16]

In this experiment the magnetic field for the sensor was produced by a superconducting wire wound coil, which was surrounding the SQUID chip. Therefore the entire SQUID chip, with Josephson junctions, was located in a field of about 2 mT. In such a field the critical current of the detector SQUID is reduced from 8 μA to about 2 μA, which results in a voltage swing ΔV of only 7 μV. This, in turn, translates into a slope of the characteristic curve of $20\,\mu\mathrm{V}/\Phi_0$. This low value results in a high noise level of the flux modulated SQUID used in this experiment, which in part explains the instrumental resolution of only 9 eV obtained with this detector.

The situation can be considerably improved by using a 2-stage SQUID with direct readout. In such a configuration the white-noise level of the readout can be reduced while maintaining the lower bias current of the detector SQUID by employing a second SQUID in a current-sensor configuration as a low noise amplifier, as discussed in Sect. 3.1.2. Using an amplifier SQUID from the IPHT in Jena [47], the effective white-noise level of the two-stage SQUID system was lowered to $1.1\,\mu\Phi_0/\sqrt{\mathrm{Hz}}$. As mentioned previously, this level still effects the resolution, but it is sufficiently low that the potential of MMCs for high resolution measurements can be demonstrated. The ^{55}Mn spectrum shown in Fig. 22 has been obtained with a two-stage SQUID configuration. In this experiment the X-rays were not absorbed by the magnetic sensor itself but in separate absorbers made of gold foils (each $150\,\mu\mathrm{m} \times 150\,\mu\mathrm{m} \times 5\,\mu\mathrm{m}$). The quantum efficiency for 6 keV X-rays of this thickness of Au is higher than 98%. These absorber foils were joined with the Au:Er sensors using a wedge bonder. The detector was cooled to a temperature of about 35 mK and its performance tested using a ^{55}Fe source. The spectrum shown in Fig. 22 contains the K_α and K_β lines of ^{55}Mn. Due to the high quantum efficiency of the gold absorber the spectrum is very clean indicating that very few events are not associated with the expected lines. The trigger level was set at about 100 eV in this experiment.

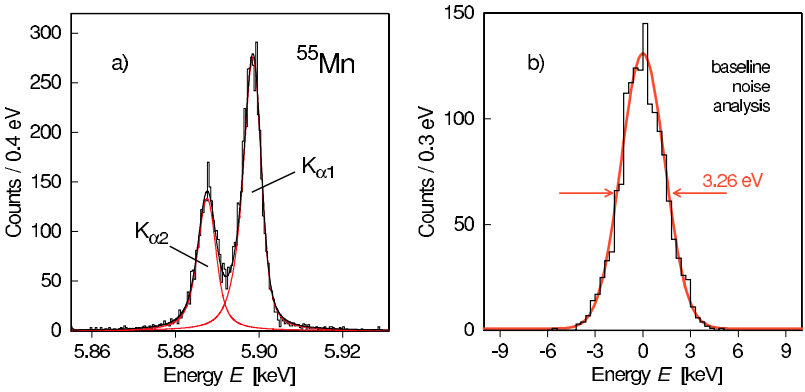

Fig. 23. (**a**) K_α line of ^{55}Mn [16]. The *solid line* represents a fit of the data taking into account the natural linewidth as determined with a crystal spectrometer [48]. (**b**) Baseline distribution determined from random noise traces without pulses, acquired simultaneously with the spectrum [16]

The *insert* of Fig. 22 shows an unfiltered single pulse. In the actual experiment a 10 Hz high pass and a 3 kHz low pass were used. The rise time of the signal is about 2 µs and, as stated before, is determined by the slew rate of the SQUID system. The thermalization time is about 60 ms due to the weak coupling to the thermal bath via vacuum grease.

To determine the instrumental resolution of the detector the K_α line was fitted with the natural line-shape as determined with a crystal spectrometer [48]. The experimental spectrum is best described with an instrumental resolution of 3.4 eV. Fig. 23a shows a blow-up of the data for the K_α line together with the theoretical spectrum taking into account the natural and instrumental linewidths. The baseline noise in this experiment was determined to be 3.26 eV by constructing a histogram from baselines (Fig. 23b) recorded at the same time as the actual spectrum. Hence, random noise dominated the instrumental resolution of the detector.

Surprisingly, the expected noise from thermodynamic fluctuations, magnetic Johnson noise and SQUID noise can only explain this baseline width in part. About half of this width is caused by the presences of an additional noise component. The spectral function of this excess noise is proportional to $1/f$. Figure 24 shows the noise spectra taken at different temperatures. It is only observed with the Au:Er sensor placed in the SQUID loop. At first glace a thermally driven $1/f$ component in a system of interacting spins might not be surprising. However, as depicted in Fig. 24, the experimentally observed $1/f$ noise is independent of temperature over almost two orders of magnitude. This puzzling feature seems to rule out most of the straight forward explanations and further experimental studies are necessary to gain more insight into the physical origin of this phenomenon. At this point is remains

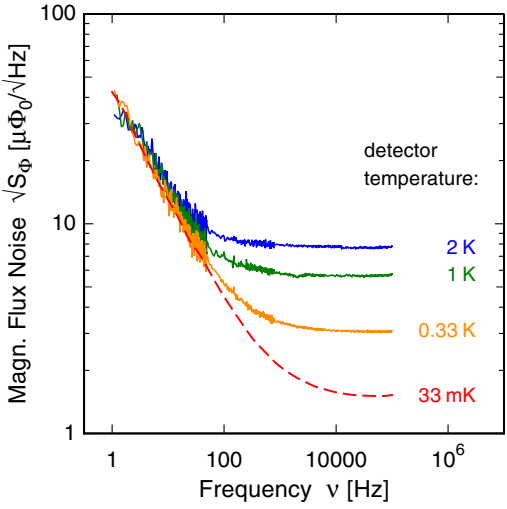

Fig. 24. Noise spectra of the high resolution detector taken at different temperatures. The *dashed line* shows the noise spectrum calculated from the baselines recorded while obtaining the X-ray spectrum shown in Fig. 23a

unclear, whether the excess $1/f$ is a fundamental property of paramagnetic alloys, or just a characteristic of Au:Er, or whether it is not caused by the material itself, but a result of the complex interplay of the electronic and thermal properties of the specific readout circuit of this experiment.

The shape of the K_β line of ^{55}Mn has been shown to depend strongly on the chemical environment in which the manganese is located [49, 50]. Using the instrumental resolution of 3.4 eV, the measured K_β line can be described satisfactorily. Fig. 25 shows the K_β line together with the theoretical spectrum of metallic manganese (*red line*) and of manganese oxide (*blue line*). The shape of the K_β line measured in this experiment is consistent with the fact that the source was metallic ^{55}Fe.

The spectrum shown in Fig. 22 can be used to determine the non-linearity of the detector. A second order polynomial fit of the peak energies reveals that the non-linearity at 6.5 keV is $\Delta E/E \approx 0.016$. The non-linearity results from the temperature dependence of the heat capacity and magnetization. The observed non-linearity agrees with calculations based on the theoretical description in Sect. 2.1.

As discussed above, the thermalization time for this prototype detector was rather slow due to the weak thermal coupling via vacuum grease between the Au:Er sensor and the SQUID chip. This thermal link can be improved dramatically by attaching the sensor to a gold pad on the SQUID chip by ultrasonic bonding or by gluing it with a small amount epoxy. In this manner thermalization times as fast as 70 μs at 50 mK have been achieved [51]. Fig. 26 shows the flux change resulting from the absorption of a 5.9 keV X-ray in a

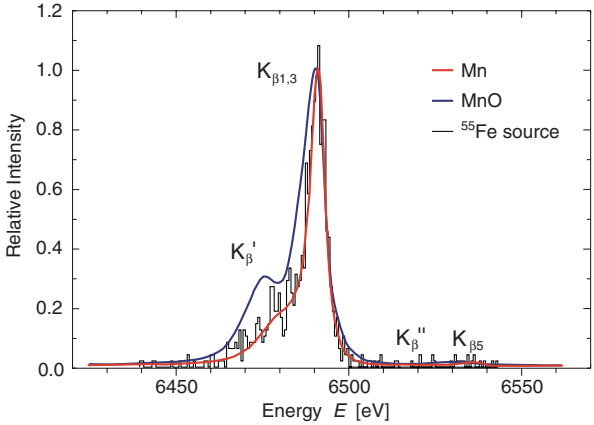

Fig. 25. K_β line of ^{55}Mn [16]. The *red line* represents a fit of the data taking into account the natural linewidth as determined with a crystal spectrometer for metallic manganese [50]. The *blue line* is the corresponding fit for MnO

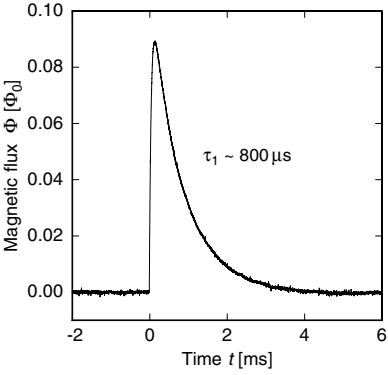

Fig. 26. Flux change caused by the absorption of a 5.9 keV X-ray photon at 50 mK in the absorber of a prototype detector in which the Au:Er sensor was glued with epoxy to the SQUID chip [51]

prototype detector in which the Au:Er sensor was glued with epoxy to the SQUID chip. In this case the thermalization time at 50 mK is approximately 1 ms. This is sufficiently fast for many applications.

3.3 Self-Inductance Magnetic Calorimeter

Recently, a MMC with planar sensor and meander-shaped pickup coil has been developed by Zink *et al.* [40]. Rather than measuring a flux change within a superconducting loop, the change in inductance of a superconducting circuit resulting from the variation of the magnetic susceptibility χ within it is used to determine the absorption of energy, as it is discussed in Sect. 2.4.4. A paramagnetic film (Au:Er) is deposited on top of a Nb meander strip which carries a moderately large current. When a particle is absorbed, the change in permeability of the paramagnetic material modifies the self-inductance of

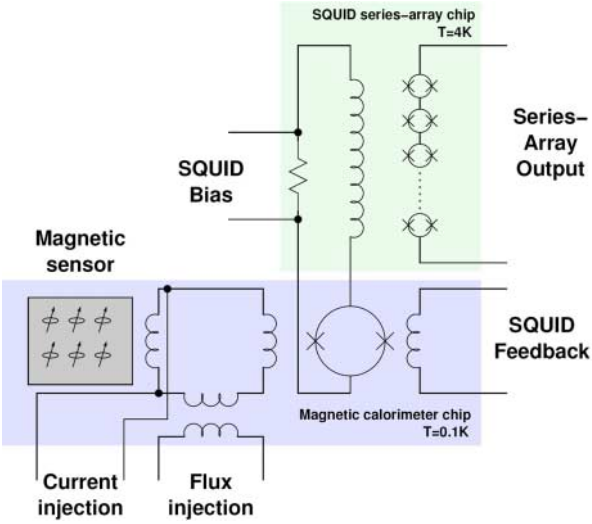

Fig. 27. Schematic of the circuit of a self-inductance MMC. After [40]

the meander line, leading to a change of the current through the SQUID that is inductively coupled to the pick-up circuit. A schematic of the circuit is shown in Fig. 27.

The dc current through the SQUID can be nulled by a flux applied through a separate coil (flux injector). Large magnetic fields at the SQUID can be avoided by ensuring that most of the injected current flows through the pick-up meander. The signal from the detector SQUID is fed to a series array SQUID for amplification.

A optical micrograph of a prototype self-inductance MMC pick-up meander is shown in Fig. 28a. A picture of the meander with a 2 µm Au:Er film deposited on top by sputtering is displayed in Fig. 28b.

Two different techniques for producing the Au:Er films have been explored, co-evaporation and sputtering. Surprisingly, the heat capacity of both types of films has turned out to be considerably larger than that measured for bulk samples having similar Er concentrations [40]. Also, the specific heat of the vapor-deposited films under the condition that $g\mu_{\mathrm{B}}B/k_{\mathrm{B}}T \ll 1$ was observed to increase with increasing temperature, which is contrary to what is expected and found for bulk samples. It should be pointed out that in the case of the self-inductance devices the magnetic field in the paramagnetic material has a rather large distribution, and a comparison using just a mean value for the field may not be very accurate. However, the qualitative and quantitative discrepancies between the heat capacity observed for films and bulk samples are so large that the field distribution cannot explain the differences. It seems likely at this point that the properties of the films themselves are responsible for the observations. A detailed understanding, however, is lacking.

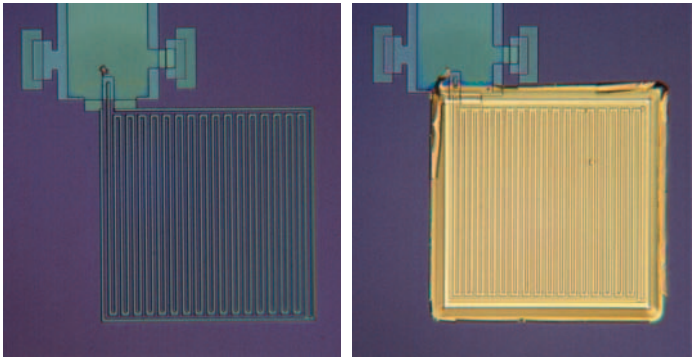

Fig. 28. Optical micrograph of a prototype MMC pick-up meander before (**a**) and after (**b**) deposition of a 2 µm Au:Er film. The detector area is about 100 µm × 100 µm. Courtesy B. Zink

The performance of the prototype self-inductance MMCs were tested using a ^{55}Fe source. As expected, the thermal coupling of the Au:Er to the SQUID was much stronger than that of sensors attached by vacuum grease, which were discussed in the previous section. The thermalization times range from 200 µs to 1 ms at 50 mK. The energy resolution obtained with a sputtered Au:Er film containing 720 ppm of natural Er was 115 eV at 6 keV. Two factors are mainly responsible for the rather poor energy resolution of these early self-inductance devices, the unexplained high heat capacity of the Au:Er film and a strong $1/f$ noise component from the electronics.

3.4 Activity Measurements in Metrology

Various fields of research such as environmental studies, nuclear waste management and geochronology require a better knowledge of the properties of radioisotopes having long half-lives or emission at low-energy. The difficulty in obtaining such information is mainly due to source self-absorption and to the dramatic decrease of detection efficiency of conventional detectors for low-energy photons and electrons. Cryogenic detectors have the potential to overcome such problems in that a detection efficiency of close to 100% is possible in the range from a few eV up to 10 keV for both X-rays and electrons.

Magnetic calorimeters have been used to demonstrate the potential of cryogenic detectors for absolute activity measurements [52, 53]. The goal of these investigations was to measure the relative activity of ^{55}Fe, decaying by electron capture from the K, L and M shells. Theoretical calculations predict that the probabilities for capture occurring from the K, L and M shells of ^{55}Fe should be 88.5%, 9.8% and 1.7%, respectively. The L captures arise almost exclusively the $L1$ sub-shell. The probability of capture from the $L2$ and $L3$ sub-shells is negligible for practical measurements. The relative probabilities

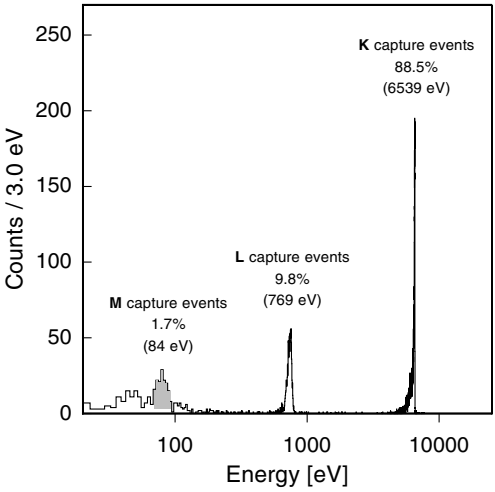

Fig. 29. Spectrum of a ^{55}Fe source fully encapsulated in a gold absorber [53]. The insert shows a schematic of the absorber/sensor arrangement

for capture from the five M sub-shells cannot be calculated reliably and are unknown experimentally. The rearrangement of the shells after the capture process is accompanied by the emission of a cascade of Auger electrons and X-rays. The total energy released in each cascade equals the binding energy of the captured electron. Therefore, if all emitted electrons and X-rays of a cascade are detected within the detector, one line is to be expected at 6.539 keV for K capture events, one line at 769 eV for L capture, and at least one line at 84 eV for M capture.

The main difficulty in performing an experiment to measure the relative probabilities is to detect the several lines at very different energies and activities with close to 100% quantum efficiency. This was achieved by enclosing the ^{55}Fe source in a gold absorber so as to record all events emitted in a 4π solid angle. A drop of ^{55}Fe in solution was deposited onto a 30 µm thick gold foil. During the drying of the drop, small crystals formed on the surface of the gold. The foil was then folded and re-laminated to a final thickness of about 20 µm. A rectangular piece of foil, $\sim 75\,\mu\text{m} \times 150\,\mu\text{m}$, fully containing the source, was cut out as the detector absorber. The effective absorber thickness was about 10 µm resulting in a quantum efficiency of over 99.9% for 6.5 keV X-rays. The absorber was then attached by ultrasonic welding to a Au:Er sensor disc (60 µm diameter, 20 µm thick) containing about 900 ppm of enriched Er. The absorber/sensor combination was placed in a SQUID loop and fixed using a small amount of vacuum grease. Because the 60 µm diameter of the sensor exceeded the 50 µm diameter of the SQUID loop, the signal size was somewhat reduced.

The detector was operated at a temperature of 25 mK in a magnetic field of about 3 mT. Figure 29 shows a spectrum on a logarithmic energy scale that was obtained by counting for about 6 hours at a count rate of

about 0.5/s. Three distinct peaks are observed, as expected. This is the first time all three capture lines have been seen in a single spectrum. To analyze the spectrum quantitatively, the K-line was used to adjust the energy scale, assuming that the detector is approximately linear up to this energy.[15] The measured energies for the M and L lines are in very good agreement with the theoretical values. The experimentally determined relative activities of the K, L and M lines are 88.2%, 10.3% and 1.5%, respectively. Within the accuracy of the experiment these values are in agreement with the theoretical calculations.

The small tails observed on the low-energy side of the K and L lines most likely originate from the absorption of Auger electrons within the source crystals, the energy not being fully transferred to the gold during the duration a typical pulse signal. It should be possible to avoid this effect by electrolytic deposition of the source material. The energy resolution of $\Delta E \approx 16\,\mathrm{eV}$ (determined from baseline noise) and the counting statistics at low energies were not sufficient to resolve a possible M shell substructure. The energy resolution was poorer than the best detector discussed in Sect. 3.2 for several reasons. The sensor/absorber heat capacity was large, the size of the sensor was not appropriate for the SQUID loop, and temperature fluctuations introduced noise because the calorimeter was not operated in a gradiometer configuration. The background at low energies is mainly the result of radioactivity in the materials surrounding the detector. We expect, that the precision of this experiment can be increased significantly by raising the activity of the source, lowering the radioactive background and improving the energy resolution of the calorimeter.

3.5 Gamma-Ray Spectroscopy

Because of the weak dependence of the sensitivity of a magnetic calorimeter on the absorber heat capacity, this type of device can be considered for applications requiring a large absorber mass, such as needed in high-resolution gamma-ray spectroscopy. Indeed, a prototype of a MMC detector for gamma rays has already been studied [54, 55, 56].

The spectrum of a ^{57}Co source as measured with a MMC detector is shown in Fig. 30a. In addition to the lines at 122 keV and 136 keV, several lines at lower energies are observed, which are due to the escape of X-ray fluorescence photons of Au. The additional broad low-count background is mostly due to electron escape processes and to gamma rays that deposit only part of their energy by Compton scattering. Note that the 14 keV line also expected for ^{57}Co was not observed in this experiment because of absorption in the material encapsulating the source.

[15] Given the large heat capacity of the absorber/sensor package this should be a good approximation

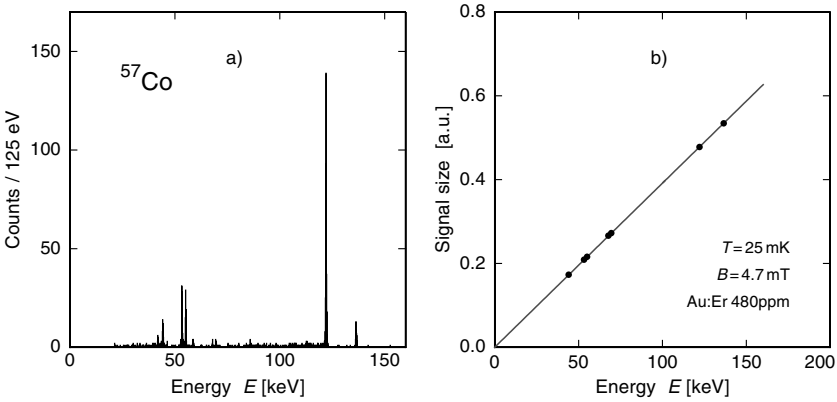

Fig. 30. (**a**) Spectrum of a ^{57}Co source measured with a prototype MMC detector operated at $T = 25\,\mathrm{mK}$ and in a magnetic field of $B = 4.7\,\mathrm{mT}$ [56]. (**b**) Measured signal size versus the energy of the expected lines in the ^{57}Co spectrum shown in (**a**) [56]

In this experiment a gold cylinder (360 µm diameter, 500 µm long) containing 480 ppm of natural erbium was used both as absorber and sensor. The quantum efficiency for detecting 122 keV gamma rays hitting directly the 500 µm thick gold is approximately 80%. At the operating conditions of $T = 25\,\mathrm{mK}$ and $B = 4.7\,\mathrm{mT}$ the heat capacity of the Au:Er cylinder is approximately $4 \times 10^{-9}\,\mathrm{J/K}$. This is more than three orders of magnitude higher than the heat capacity of the high resolution X-ray detectors discussed in Sect. 3.2.

Given the large heat capacity of the detector the absorption of a single 122 keV photon causes a temperature change in the sensor of about 5 µK, which corresponds to a relative change of $\delta T/T = 2 \times 10^{-4}$ at 25 mK. This implies that the detector exhibits a high degree of linearity up to the maximum energy recorded in this experiment. This is demonstrated in a plot of the measured pulse heights of the ^{57}Co gamma ray lines and the known escape peaks of Au as a function of their energies, as shown in Fig. 31b. No deviation from linearity outside of the experimental error of 5×10^{-4} was found. The calculated non-linearity is an order of magnitude smaller than this.

The Au:Er cylinder was located inside a 32-turn coil of superconducting wire, which was connected to the input coil of a commercial, flux-modulated SQUID to form a superconducting flux transformer. Since the Au sensor was spot-welded to a large block of copper, which served as the thermal reservoir, the thermalization time was approximately 200 µm. A signal produced by a single 122 keV gamma ray is shown in Fig. 30a.

The energy resolution determined by the FWHM of the line at 122 keV is 340 eV. The two main broadening mechanisms of approximately equal im-

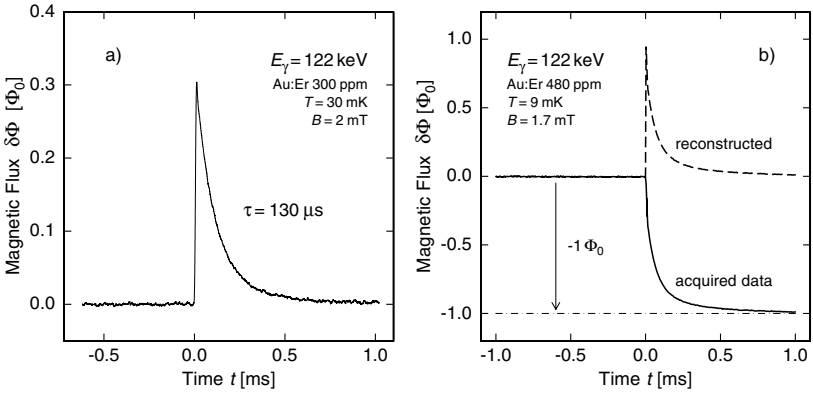

Fig. 31. (**a**) Signal resulting from the absorption of a single 122 keV gamma ray. (**b**) The *solid line* shows a single 122 keV event with $\Phi < 0.5\,\Phi_0$ as recorded with a SQUID electronics with a slew rate of $20\,\Phi_0$/ms. The *dashed line* shows the reconstructed pulse after recalculation of the working point [57]

portance are random noise at low frequencies, as determined from baseline traces, and insufficient temperature stability of the cryostat. The incoherent sum of the noise from these two sources accounts almost entirely for the observed energy resolution.

Due to the use of a flux transformer the sensitivity of the detector was somewhat reduced. However, this was not an important limitation is this experiment because the slew rate ($20\,\Phi_0$/ms) of the SQUID electronics restricted the size of the flux changes to about $0.5\,\Phi_0$. With larger signals, flux jumps occurred, which prohibited an accurate determination of the total flux change. Under optimal conditions the signal size from the 122 keV gamma ray was considerably larger than Φ_0. A typical event with flux jump is shown in Fig. 31b.

The prototype gamma ray detector discussed in this section was not optimized for a specific application, but was used to demonstrate the potential of MMCs in gamma ray detection. An optimized detector would include an absorber. To give a specific example of the capabilities of a optimized detector we assume an absorber with a heat capacity of $C_a = 1$ nJ/K, a value which is similar to that of the prototype detector and corresponds roughly to a gold absorber of $(650\,\mu\text{m})^3$. In addition, we assume an operational temperature of $T = 50$ mK and relaxation times of $\tau_0 = 1\,\mu$s and $\tau_1 = 1$ ms as in the example discussed in Sect. 3.2. Such a detector is expected to have an intrinsic energy resolution of about $\Delta E_{\text{FWHM}} = 60$ eV.

4 Summary and Outlook

We have discussed the basic thermodynamic properties of metallic magnetic calorimeters and the paramagnetic sensor material. Furthermore, a model has been presented which allows for the optimization of the signal to SQUID noise ratio for different detector geometries. Based on these findings, the principle limitations of the energy resolution of metallic magnetic calorimeters have been discussed and guidelines for the design of MMCs with optimized energy resolution have been derived. Results obtained with several prototype detectors have been presented.

Magnetic calorimeters have reached a level of development at which many interesting applications are conceivable. However, several important issues will need to be addressed in the further development of MMC detectors: 1. Suitable techniques are required for the micro-fabrication of fully integrated MMC detectors. In this context it will be necessary to study the magnetic properties of thin paramagnetic films produced by sputtering or vapor deposition techniques. 2. The origin of the unexplained $1/f$ excess noise needs to be investigated. If this noise contribution cannot be sufficiently reduced, it will likely be a limiting factor in the energy resolution of MMCs. To investigate the origin of $1/f$ noise, the properties of temperature sensors based on other paramagnetic materials need to be studied. 3. Advanced readout schemes including multiplexing techniques have to be developed to allow for large MMC arrays. Although the underlying physics of MMC and TES detectors is quite different it seems conceivable that the development of SQUID based multiplexing schemes for MMCs can benefit to a large extent from the enormous progress that has been made in multiplexing TES detectors.

These and many other aspects of magnetic calorimeters have to be investigated to make use of the full potential of this kind of cryogenic detector.

Acknowledgements

We would like to thank S.R. Bandler, J. Beyer, H.F. Braun, A. Burck T. Daniyarov, D. Drung, H. Eguchi, S. Hunklinger, K.D. Irwin, Y.-H. Kim, E. Leblanc, M. Linck, M. Loidl, H.-G. Meyer, H. Rotzinger, J. Schönefeld, M.v. Schickfus, R. Stolz, V. Zakosarenko, and B.L. Zink for many useful and stimulating discussions.

References

[1] T.C.P. Chui, D.R. Swanson, M.J. Adriaans, J.A. Nissen, J.A. Lipa: Phys. Rev. Lett. **69**, 3005 (1992). 151
[2] P. Day, I. Hahn, T.C.P. Chui, A.W. Harter, D.Rowe, J.A. Lipa: J. Low Temp. Phys. **107**, 1 (1997). 151
[3] P.B. Welander, I. Hahn: Rev. Sci. Instrum. **72**, 3600 (2001). 151

[4] B.J. Klemme, M.J. Adriaans, P.K. Day, D.A. Sergatskov, T. L. Aselage, R.V. Duncan: J. Low Temp. Phys. **116**, 133 (1999). 151
[5] W. Seidel: Diploma Thesis, Technische Universität München 1986, unpublished. 151
[6] M. Bühler, E. Umlauf: Europhys. Lett. **5**, 297 (1988) 152, 154
[7] E. Umlauf, M. Bühler: Proc. Symp. Supercon. and Low-Temp. Detectors, eds. G. Waysand and G. Chardin, 309 (North-Holland, Amsterdam 1989). 152, 154
[8] E. Umlauf, M. Bühler: Proc. Int. Workshop on Low Temperature Detectors for Neutrino and Dark Matter (LTD4), eds. N.E. Booth and G.L. Salmon, 229 (Editors Frontieres, Gir-sur-Yvette 1991). 152, 154
[9] M. Bühler, E. Umlauf: Proc. Int. Workshop on Low Temperature Detectors for Neutrino and Dark Matter (LTD4), eds. N.E. Booth and G.L. Salmon, 237 (Editors Frontieres, Gir-sur-Yvette 1991). 152, 154
[10] E. Umlauf, M. Bühler: Proc. SPIE Conference **1743**, 391 (San Diego 1992). 152, 154
[11] M. Bühler, E. Umlauf, D. Drung, H. Koch: Proc. 5th Int. Conf. on Supercon. Quantum Devices and their Application, eds. H. Koch and H. Lübbig (Springer, Heidelberg 1992) 152, 154
[12] M. Bühler, T. Fausch, E. Umlauf: Europhys. Lett. **23**, 529 (1993) 152, 154
[13] E. Umlauf, M. Bühler, T. Fausch: Proc. Phonon Scattering in Condensed Matter VII, eds. M. Meissner and R.O. Pohl, (Springer, Berlin 1993). 152, 154
[14] T. Fausch, M. Bühler, E. Umlauf: J. Low Temp. Phys. **93**, 703 (1993). 152, 154
[15] S.R. Bandler, C. Enss, R.E. Lanou, H.J. Maris, T. More, F.S. Porter, and G.M. Seidel: J. Low Temp. Phys. **93**, 709 (1993). 152, 154
[16] A. Fleischmann, M. Linck, T. Daniyarov, H. Rotzinger, C. Enss, G.M. Seidel: Nucl. Instr. Meth. A**520**, 27 (2004). 152, 204, 205, 207
[17] A.H. Cooke, H.J. Duffus, W.P. Wolf: Phil. Mag. **44**, 623 (1953). 153
[18] P.G. de Gennes: Comp. Rend. Acad. Sci. **247**, 1836 (1966). 154
[19] M. Bühler, E. Umlauf, K. Winzer: Nucl. Inst. Meth. Phys. A **370**, 621 (1996). 155
[20] M. Böe: Diploma thesis, Universität Heidelberg 1998, unpublished. 155
[21] C. Enss, A. Fleischmann, T. Görlach, Y.H. Kim, G.M. Seidel, H.F. Braun: AIP Conference Proceedings **605**, 71 (2002). 155
[22] G. Williams and L.L. Hirst: Phys. Rev. **185**, 407 (1969). 155
[23] L.J. Tao, D. Davidov, R. Orbach, and E.P. Chock: Phys. Rev. B**4**, 5 (1971). 155, 163
[24] M.E. Sjöstrand and G. Seidel: Phys. Rev. B**11**, 3292 (1975). 155, 161
[25] D. Davidov, C. Rettori, A. Dixon, K. Baberschke, E.P. Chock, and R. Orbach: Phys. Rev. B**8**, 3563 (1973). 155
[26] W. Hahn, M. Loewenhaupt and B. Frick: Physica B**180&181**, 1698 (2000). 155
[27] T. Herrmannsdörfer, R. König and C. Enss: Physica B **284-288**, 1698 (2000). 155
[28] A. Fleischmann: PhD Thesis, Universität Heidelberg, (2003). 155, 156, 177
[29] L.R. Walker and R.E. Walsted: Phys. Rev. Lett. **38**, 514 (1977). 158

[30] L.R. Walker and R.E. Walsted: Phys. Rev. B**22**, 3816 (1980). 158
[31] S. Arajs and G.R. Dunmyre: J. Less-Common Metals **10**, 220 (1966); see also L. R. Edwards and S. Levgold, J. Appl. Phys. **39**, 3250 (1968). 158, 187
[32] C. Enss, A. Fleischmann, K. Horst, J. Schönefeld, J. Sollner, J.S. Adams, Y.H. Huang, Y.H. Kim, G.M. Seidel: J. Low Temp. Phys. **121**, 137 (2000). 159, 160, 164, 174, 177, 178, 187
[33] A. Fleischmann, C. Enss, J. Schönefeld, J. Sollner, K. Horst, J.S. Adams, Y.H. Kim, G.M. Seidel, S.R. Bandler: Nucl. Instr. Meth. A**444**, 100 (2000) 163
[34] K. Konzelmann, G. Majer, and A. Seeger: Z. Naturforsch. A**51**, 506 (1996). 163
[35] M. Minier and C. Minier: Phys. Rev. B**22**, 21 (1980). 163
[36] B. Perscheid, H. Büchsler, M. Forker: Phys. Rev. B**14**, 4803 (1976). 163
[37] J. Souletie, R. Tournier: J. Low Temp. Phys. **1**, 95 (1969). 163
[38] *The SQUID Handbook* edited by J. Clarke and A.I. Braginski, ISBN 3-527-40229-2, Wiley-VCH (2004). 168, 169
[39] H. Seppä, M. Kiviranta and L. Grönberg: IEEE Tran. Appl. Supercond. **5**, 3248, (1995). 171
[40] B.L. Zink, K.D. Irwin, G.C. Hilton, D.P. Pappas, J.N. Ullom, M.E. Huber: Nucl. Instr. Meth. B **520**, 52 (2003). 173, 207, 208
[41] T. Varpula and T. Poutanen: J. Appl. Phys. **55**, 4015 (1984), see also B.J. Roth, J. Appl. Phys. **83**, 635 (1998). 187
[42] D.T. Gillespie: J. Appl. Phys. **83**, 3118 (1998). 187
[43] J.T. Harding and J.E. Zimmerman: Phys. Lett. A **27**, 670 (1968). 187
[44] A. Fleischmann: Adv. Solid State Phys. **41**, 577 (2001) 196
[45] M.B. Ketchen, D.D. Awschalom, W.J. Gallagher, A.W. Kleinsasser, R.L. Sandstrom, J.B. Rosen, B. Bumble: IEEE Trans. Mag. **25**, 1212 (1989). 202
[46] A. Fleischmann, T. Daniyarov, H. Rotzinger, C. Enss, G.M. Seidel: Physica B **329-333**, 1594 (2003). 203
[47] M.A. Espy, A.N. Matlachov, R.H. Kraus, and J.B. Betts: IEEE Tran. Appl. Supercond. **13**, 731, (2003). 204
[48] G. Hölzer, M. Fritsch, M. Deutsch, J. Hartwig, and E. Förster: Phys. Rev. A **56**, 4554 (1997). 205
[49] K. Tsutsumi, H. Nakamoi, K. Ichikawa: Phys. Rev. B **13**, 929 (1976). 206
[50] K. Sakurai, H. Eba: Nucl. Instr. Meth. B **199**, 391 (2003). 206, 207
[51] T. Daniyarov, C. Enss, A. Fleischmann, M. Linck, H. Rotzinger, G.M. Seidel: to be published. 206, 207
[52] M. Loidl, E. Leblanc, J. Bouchard, T. Branger, N. Coron, J. Leblanc, P. de Marcillac, H. Rotzinger, T. Daniyarov, M. Linck, A. Fleischmann, C. Enss: Appl. Rad. Isotopes **60**, 363 (2004). 209
[53] M. Loidl, E. Leblanc, T. Branger, H. Rotzinger, T. Daniyarov, M. Linck, A. Fleischmann, C. Enss: Nucl. Instr. Meth. B **520**, 73 (2004). 209, 210
[54] S.R. Bandler, C. Enss, J. Schönefeld, L. Siebert, G.M. Seidel, R. Weis: *Proceedings of the 7th International Workshop on Low Temperature Detectors LTD-7*, (S. Cooper ed.), 145 (1997). 211
[55] J.S. Adams, S.R. Bandler, C. Enss, A. Fleischmann, Y.H. Huang, H.Y. Kim, J. Schönefeld, G.M. Seidel, R. Weis: *Proceedings of the International Symposium on Optical Science and Technology (SPIE)* **4140**, 445 (2001). 211

[56] A. Fleischmann, C. Enss, J. Schönefeld, J. Sollner, K. Horst, J.S. Adams, Y.H. Kim, G.M. Seidel, S.R. Bandler: Nucl. Instr. and Meth. A **444**, 211 (2000). 211, 212

[57] C. Enss: AIP Conference Proceedings **605**, 5 (2002). 213